Electronic Supplementary Material (ESI) for Dalton Transactions.
This journal is © The Royal Society of Chemistry 2024

Supplementary Material

From field-induced to zero-field SMMs associated with open/closed structures of bis(ZnDy) tetranuclear complexes: a combined magnetic, theoretical and optical study

Andoni Zabala-Lekuona,*[a] Xabier Lopez de Pariza,[b] Ismael F. Díaz-Ortega,[c,d] Javier Cepeda,[a] Hiroyuki Nojiri,[d] Nina P. Gritsan,[e] Alexey A. Dmitriev,[e] Alberto López-Ortega,[f,g,h] Antonio Rodríguez-Diéguez,[i] José M. Seco*[a] and Enrique Colacio*[i]

[a]*Departamento de Química Aplicada, Facultad de Química, Universidad del País Vasco (UPV/EHU), 20018 Donostia-San Sebastián, Spain. Email: andoni.zabala@ehu.eus; josemanuel.seco@ehu.eus*

[b]*POLYMAT and Department of Polymers and Advanced Materials: Physics, Chemistry and Technology, Faculty of Chemistry, University of the Basque Country UPV/EHU, Paseo Manuel de Lardizabal 3, Donostia-San Sebastián 20018, Spain*

[c]*Departamento de Química y Física-CIESOL, Universidad de Almería, Ctra. Sacramento s/n, 04120 Almería, Spain*

[d]*Institute for Materials Research, Tohoku University, Katahira, Sendai, 980-8577, Japan*

[e]*Institute of Chemical Kinetics and Combustion, Siberian Branch, Russian Academy of Sciences, 630090 Novosibirsk, Russia*

[f]*Departamento de Ciencias, Universidad Pública de Navarra, E-31006 Pamplona, Spain*

[g]*Institute for Advanced Materials and Mathematics (INAMAT^2), Universidad Pública de Navarra, E-31006 Pamplona, Spain*

[h]*CIC nanoGUNE BRTA, Tolosa Hiribidea 76, Donostia-San Sebastian, 20018, Spain*

[i]*Departamento de Química Inorgánica, Facultad de Ciencias, Universidad de Granada, 18071 Granada, Spain. Email: ecolacio@ugr.es*

Contents:

S1.- Experimental and computational procedures

S2.- Elemental analysis

S3.- ICP-MS analysis

S4.- Crystallographic tables

S5.- Continuous Shape Measurements (CShM)

S6.- Additional figures

S7.- Static magnetic properties

S8.- Dynamic magnetic properties

S9.- Theoretical calculations

S10.- Photoluminescence properties

S11.- Powder X-ray diffraction analysis

S12.- Nuclear Magnetic Resonance

S13.- References

S1.- Experimental and computational procedures

Synthetic procedures

General procedures: All reactions were conducted in oven-dried glassware under aerobic conditions. All analytical grade reagents were purchased from commercial sources and used without further purification.

Synthesis of ligand H_4L (1,4,8,11-tetraaza-1,4,8,11-tetrakis(2-hydroxy-3-methoxy-5-methylbenzyl) cyclotetradecane

A mixture of 1,4,8,11-tetraazacyclotetradecane (10 mmol, 2.00 g) and paraformaldehyde (44 mmol, 1.32 g) was refluxed in 15 mL of methanol for 1.5 h. At this time, 2-methoxy-4-methylphenol (44 mmol, 5.59 mL) was added to the solution and was refluxed for other 24 h. The white mixture was cooled to room temperature and the solid was filtered, washed with methanol and dried under vacuum yielding pure H_4L. Yield: 90%.

^{1}H-NMR (500 MHz, $CDCl_3$, ppm, Figure S93): 6.59 (s, 4H, aryl-*H*), 6.35 (s, 4H, aryl-*H*), 3.83 (s, 12H, OCH_3), 3.61 (s, 8H, aryl-CH_2N), 2.76 (s, 8H, NCH_2CH_2N), 2.60 (t, ^3J = 7.3 Hz, 8H, NCH_2CH$_2$CH_2N), 2.20 (s, 12H, aryl-CH_3), 1.81 (p, ^3J = 7.6 Hz, 4H, NCH$_2$CH_2CH$_2$N).

Synthesis of $[Zn_2(\mu\text{-}L)(\mu\text{-}OAc)Dy_2(NO_3)_2]\cdot[Zn_2(\mu\text{-}L)(\mu\text{-}OAc)Dy_2(NO_3)(OAc)]\cdot 4CHCl_3\cdot 2MeOH$ (1)

To a solution of H_4L (0.04 mmol, 32.0 mg) and Et_3N (0.16 mmol, 0.02 mL) in 10 mL of chloroform was added a methanol solution (10 mL) containing $Zn(OAc)_2\cdot 2H_2O$ (0.08 mmol, 17.6 mg) and $Ln(NO_3)_3\cdot xH_2O$ (0.08 mmol). The resulting colourless solution was allowed to stand at room temperature and in few days, suitable crystals for X-ray diffraction were obtained. Note that two slightly different molecules cocrystallize within the crystal structure (see crystal structure description). Yield and elemental analysis results in Table S1.

Synthesis of $[TM_2(\mu\text{-}H_2L)_2(\mu\text{-succinate})Ln_2(NO_3)_2](NO_3)_2\cdot 2H_2O\cdot 6MeOH$ (TM^{II} = Zn, Ln^{III} = Dy (2); TM^{II} = Co, Ln^{III} = Dy (3))

To a solution of H_4L (0.04 mmol, 32.0 mg), $TM(NO_3)_2\cdot xH_2O$ (0.04 mmol) and $Ln(NO_3)\cdot xH_2O$ (0.04 mmol) in 20 mL of methanol was added dropwise another solution containing succinic acid (0.02 mmol, 2.4 mg) and Et_3N (0.12 mmol, 0.016 mL) in 1 mL of methanol. A thin powder was formed after the addition of each drop, but it easily got

dissolved. The solution was stirred for few seconds, filtered in order to remove possible undissolved particles and allowed to stand at room temperature. In few days, suitable crystals for X-ray diffraction were obtained. Yield and elemental analysis results in Table S1.

Synthesis of magnetically diluted $\mathbf{1_Y}$, $\mathbf{2_Y}$, $\mathbf{3_{Zn}}$, and $\mathbf{3_Y}$

In the case of $\mathbf{1_Y}$ and $\mathbf{2_Y}$ the paramagnetic Ln^{III} ions were diluted with the diamagnetic Y^{III} counterpart. In the case of **3**, however, both paramagnetic ions were diluted separately, Co^{II} with Zn^{II} and Dy^{III} with Y^{III} yielding $\mathbf{3_{Zn}}$ and $\mathbf{3_Y}$, respectively. In all cases, diluted derivatives were synthesized following the same experimental procedure, but with Ln:Y and Co:Zn molar ratios of 1:10.

ICP-MS analysis

The sample preparation for ICP-MS analysis was based on a microwave assisted acid digestion. For that purpose, few milligrams (4-10 mg) of sample were dissolved in 1 mL of HNO_3 and the solutions were digested in the microwave following the Ruthenium Alloys method. Subsequently, samples were diluted using diluted aqua regia to a volume of 3 mL and the analysis of different elements was carried out by ICP-MS.

An iCAP-Q ICP-MS (Thermo Scientific, Bremen, Germany) instrument was employed equipped with an automatic sampler ASX-500 (CETAC Technologies, Omaha, USA). On the one hand, the quantification of Co and Zn elements was carried out by using Qtegra v2.6 software (ThermoFisher, Bremen, Germany) monitoring ^{59}Co and ^{64}Zn isotopes and using ^{115}In as internal standard. On the other hand, Y and Dy were analysed by monitoring ^{89}Y and ^{163}Dy isotopes and using ^{193}Ir as internal standard.

Physical measurements

Elemental analyses (C, H, N) were performed on a Leco CHNS-932 microanalyzer. Magnetic susceptibility measurements were carried out on polycrystalline samples of the complexes with a Quantum Design SQUID MPMS-7T magnetometer at an applied magnetic field of 1000 G. The susceptibility data were corrected for the diamagnetism estimated from Pascal's Tables,[1] the temperature-independent paramagnetism, and the magnetization of the sample holder. Alternating current measurements were performed on a Quantum Design PPMS-6000 magnetometer under a 3.5 G ac field and frequencies ranging from 60 to 10000 Hz.

Pulse-field magnetization

Low-temperature magnetization measurements were performed by means of a conventional inductive probe in pulsed-magnetic fields. The temperature was reached as low as 0.4 K using a ^{3}He cryostat.[2] Polycrystalline specimens were mounted in a polyimide capillary tube. Samples of approximately 20 mg were not fixed inside the sample tube and then they aligned along the magnetic field direction. Subsequently, the magnetic field was applied several times until the orientation effect was saturated and the magnetization curves obtained in the next shots were found to be identical.

X-ray diffraction data collection and structure determination

Suitable single crystals of the ligand H_4L and compounds **1** and **3** were mounted on a Bruker D8 VENTURE diffractometer equipped with area detector and graphite monochromated MoK_α radiation (λ = 0.71073 Å). Instead, compound **2** was measured on an Agilent Technologies Super Nova diffractometer with monochromatic CuK_α radiation (λ = 1.54184 Å) and an Atlas CCD detector. Data collection was performed by applying the ω-scan method used for the structure determination at temperatures that are indicated in Table S2. Data reduction was performed with the APEX2[3] software and absorption was corrected using SADABS.[4] Crystal structures were solved by intrinsic phasing using the SHELXT program[5] and refined by full-matrix least squares on F^2 including all reflections employing the WINGX crystallographic package.[6,7] The main crystallographic details and refinement data may be found in Table S3. During the refinement process of compounds **1** and **2** the solvent molecules were clearly visible, but were not assigned due to the large disorder. Therefore, the structures were resolved with a squeeze routine. In the case of **3**, however, a reasonable model was obtained with the mentioned crystallization molecules. Crystallographic data has been deposited with the Cambridge Crystallographic Data Centre as supplementary publication with no. CCDC 2226682–2226685.

The X-ray powder diffraction (XRPD) patterns were measured on pre-ground single crystals (Figures S88-S92). For data acquisition, a Philips X'PERT powder diffractometer was used with Cu-Kα radiation (λ = 1.5418 Å) over the range $5 < 2\theta < 50°$ with a step size of 0.026° and a data acquisition time of 2.5 s per step at 25 °C.

Computational methodology

Complex **1** consists of two types of tetranuclear bis(ZnDy) clusters with long intracluster distances between Dy^{III} cations (12.105 and 12.301 Å), which are even longer than shortest Dy-Dy intercluster distances (9.067 Å). Thus, for calculations, we divided both bis(ZnDy) clusters into binuclear DyZn clusters by cutting the middle C-C bonds of N-$(CH_2)_3N$ chains connecting two Zn^{II} cations and adding a hydrogen atom to the CH_2 group of one of them and discarding the other DyZn cluster. These binuclear complexes were named **1′A** and **1′B**.

In the case of complexes **2**, the only type of tetranucleat bis(ZnDy) clusters also has rather large intracluster Dy-Dy distances (8.699 Å). Therefore, for calculations, we also divided this cluster into two DyZn binuclear units by breaking five C-C bonds and adding five hydrogen atoms to one of them and discarding the other. Binuclear complexes are called **2′**.

The tetranuclear cluster (bis(CoDy)) of **3** contains four paramagnetic cations with sufficiently large intracluster distances Dy-Dy (8.75 Å) and Co-Co (7.66 Å). As in the case of **2**, tetranuclear cluster of **3** was split into two binuclear DyCo (**3′**) complexes by breaking five C-C bonds. However, in the case of **3′**, *ab initio* calculations were carried out for analogues of **3′** with the replacement of the Dy^{III} cation by Y^{III} ($\mathbf{3'_Y}$) and with the replacement of the Co^{II} cation by Zn^{II} ($\mathbf{3'_{Zn}}$). The magnetic properties of complex **3′** were calculated using the results of *ab initio* calculations for $\mathbf{3'_{Zn}}$ and $\mathbf{3'_Y}$ and taking into account the dipole-dipole and exchange interactions between paramagnetic Dy^{III} and Co^{II} cations.

For all *ab initio* electronic structure calculations discussed in this paper, the OpenMolcas program[8,9] (version 19.11) was used. For complexes containing Dy^{III} and Zn^{II} cations (**1′A**, **1′B**, **2′** and $\mathbf{3'_{Zn}}$), the electronic energies and wave functions of spin multiplets (21 sextets, 128 quartets, and 130 doublets) were calculated at the state-averaged[10] (SA) CASSCF(9,7) level[11,12] (active space: nine electrons distributed over the seven f-orbitals of Dy) with the relativistic ANO-RCC-VTZP basis set for Dy and O atoms of coordination sphere and the smaller ANO-RCC-VDZ basis set for other atoms.[13] Scalar relativistic effects were taken into account using the DKH2 Hamiltonian.[14,15] The spin–orbit coupling was treated non-perturbatively within the mean-field theory in the restricted active space state interaction (SO-RASSI) method,[16,17] in which the CASSCF

wave functions are used as the basis states. Diagonalization of the spin–orbit matrix leads to spin-orbit multiplets (Kramers doublets for above mentions Dy^{III} complexes).

For the $\mathbf{3'_Y}$ complex containing the paramagnetic Co^{II} cation, the electronic structure calculations were performed at the SA-CASSCF(7,5)/SO-RASSI level using the ANO-RCC-VTZP basis set for Co, N and O atoms of the coordination sphere and the ANO-RCC-VDZ basis set for all other atoms. The SA-CASSCF(7,5) (active space: seven electrons distributed over the five d-orbitals of Co cation) calculations took into account 10 quintet and 40 doublet states and predicted that seven lowest spin multiplets of this cluster are quintet states.

To calculate parameters of the effective spin (pseudospin) Hamiltonians (g-tensors, their principal values, angular momenta along the principal magnetic exes, matrix elements of the transverse magnetic moment, etc.) and the static magnetic properties of complexes with one magnetic nucleus (all the considered complexes, excluding $\mathbf{3'}$), the SINGLE_ANISO program was used.[18,19]

The POLY_ANISO program[20] was used to calculate the electronic structure, parameters of pseudospin Hamiltonian, and static magnetic properties of the $\mathbf{3'}$ complex containing two paramagnetic cations. The POLY_ANISO module performs calculations of the anisotropic exchange interaction (within the framework of the Lines model)[21] and dipole–dipole magnetic interaction between Dy^{III} and Co^{II} centers using *ab initio* calculated wave functions and spectrum of the $\mathbf{3'_{Zn}}$ and $\mathbf{3'_Y}$ complexes.

S2.- Elemental analysis

Table S1.- Yields and elemental analyses for complexes **1-3**.

Complex	Yield (%)	Formula	% C calc./found	% H calc./found	% N calc./found
1	28	$C_{110}H_{150}Cl_{12}N_{14}O_{48}Zn_4Dy_4$	35.01/35.25	4.01/4.00	5.20/5.12
2	61	$C_{102}H_{156}N_{12}O_{40}Zn_2Dy_2$	46.30/46.35	5.94/6.03	6.35/6.27
3	46	$C_{102}H_{156}N_{12}O_{40}Co_2Dy_2$	46.52/46.66	5.97/6.26	6.38/6.12

S3.- ICP-MS analysis

Table S2.- ICP-MS results for diluted compounds **1_Y**, **2_Y**, **3_{Zn}** and **3_Y**. The equivalents are obtained by dividing the concentration (μg/L) with the atomic weight. The ratio is obtained by dividing equivalents.

	μg/L				**Equivalents**				**Ratio**	
	Y	**Dy**	**Zn**	**Co**	**Y**	**Dy**	**Zn**	**Co**	**Y/Dy**	**Zn/Co**
1_Y	163623.62	28472.10	-	-	1840.54	175.21	-	-	10.50	-
2_Y	92011.50	16746.42	-	-	1035.00	103.05	-	-	10.04	-
3_{Zn}	-	-	56722.28	4818.05	-	-	867.31	81.80	-	10.60
3_Y	264338.83	52191.25	-	-	2973.44	321.18	-	-	9.26	-

S4.- Crystallographic tables

Table S3.- Crystallographic data for H_4L and compounds **1-3**.

Structure	**H_4L**	**1**	**2**	**3**
Formula	$C_{46}H_{64}N_4O_8$	$C_{110}H_{150}Cl_{12}N_{14}O_{48}Zn_4Dy_4$	$C_{102}H_{156}N_{12}O_{40}Zn_2Dy_2$	$C_{102}H_{156}N_{12}O_{40}Co_2Dy_2$
M_r	801.01	3773.31	2646.12	2633.24
Crystal system	*triclinic*	*monoclinic*	*orthorhombic*	*orthorhombic*
Space group (no.)	*P*-1 (2)	*P* 2/*c* (13)	*Pba*2 (32)	*Pba*2 (32)
a (Å)	7.7203(4)	22.4610(7)	20.89300(10)	20.934(2)
b (Å)	11.3727(5)	11.6306(4)	22.74300(10)	22.821(2)
c (Å)	12.6080(6)	26.5609(9)	12.2250(8)	12.2957(13)
α (°)	91.3198(17)	90	90	90
β (°)	103.0343(16)	97.4880(10)	90	90
γ (°)	100.5413(18)	90	90	90
V (Å^3)	1057.88(9)	6879.5(4)	5808.9(4)	5874.2(10)
Z	1	2	2	2
D_c (g cm^{-3})	1.257	1.822	1.513	1.489
μ(MoK$_\alpha$) (mm^{-1})^d	0.086	3.151	7.970	1.622
T (K)	100(2)	100(2)	150.00(10)	100(2)
Observed reflections	5476 (4032)	17844 (16076)	11050 (10714)	13908 (11122)
R_{int}	0.0667	0.0489	0.0609	0.0774
Parameters	266	796	659	735
GOF	1.047	1.144	1.106	1.128
R_1[a,b]	0.0852 (0.0562)	0.0424 (0.0359)	0.0403 (0.0389)	0.0985 (0.0678)
wR_2[c]	0.1347 (0.1226)	0.0774 (0.0754)	0.0904 (0.0898)	0.1714 (0.1516)
Largest difference in peak and hole (e Å^{-3})	0.400 and -0.349	1.522 and -1.625	0.798 and -1.557	3.298 and -2.848

[a]$R_1 = \Sigma||F_o| - |F_c||/\Sigma|F_o|$. [b]Values in parentheses for reflections with $I > 2\sigma(I)$. [c]$wR_2 = \{\Sigma[w(F_o^2 - F_c^2)^2]/\Sigma[w(F_o^2)^2]\}^{½}$. [d] μ(CuK$_\alpha$) (mm^{-1}) in **2**.

Table S4.- Bond lengths (Å) and angles (°) for compound **1**.

Compound	**1A**		**1B**
Dy1A···Zn1A	3.3884(4)	Dy1B···Zn1B	3.4009(4)
Dy1A-O1A	2.262(2)	Dy1B-O1B	2.274(2)
Dy1A-O2A	2.563(3)	Dy1B-O2B	2.515(2)
Dy1A-O3A	2.278(2)	Dy1B-O3B	2.285(2)
Dy1A-O4A	2.547(3)	Dy1B-O4B	2.572(2)
Dy1A-O1C	2.329(3)	Dy1B-O1D	2.346(3)
Dy1A-O5A	2.466(3)	Dy1B-O5B	2.452(3)
Dy1A-O6A	2.441(3)	Dy1B-O6B	2.500(3)
Dy1A-O8A	2.449(3)	Dy1B-O8B	2.407(3)
Dy1A-O9A	2.486(3)	Dy1B-O9B	2.441(3)
Zn1A-N1A	2.143(3)	Zn1B-N1B	2.140(3)
Zn1A-N2A	2.181(3)	Zn1B-N2B	2.221(3)
Zn1A-O1A	2.064(2)	Zn1B-O1B	2.055(2)
Zn1A-O3A	2.040(3)	Zn1B-O3B	2.007(2)
Zn1A-O2C	1.977(3)	Zn1B-O2D	1.969(2)
Dy1A-O1A-Zn1A	103.01(10)	Dy1B-O1B-Zn1B	103.41(10)
Dy1A-O3A-Zn1A	103.27(10)	Dy1B-O3B-Zn1B	104.63(10)
O1A-Dy1A-O3A	65.67(9)	O1B-Dy1B-O3B	64.56(8)
O1A-Dy1A-O1C	82.05(9)	O1B-Dy1B-O1D	81.76(9)
O3A-Dy1A-O1C	82.11(9)	O3B-Dy1B-O1D	79.45(9)
O1A-Zn1A-O3A	73.72(10)	O1B-Zn1B-O3B	73.65(9)
O1A-Zn1A-O2C	100.11(11)	O1B-Zn1B-O2D	98.56(10)
O3A-Zn1A-O2C	102.79(11)	O3B-Zn1B-O2D	104.83(10)
N1A-Zn1A-N2A	85.25(12)	N1B-Zn1B-N2B	85.76(10)

Table S5.- Bond lengths (Å) and angles (°) for compounds **2** and **3** (TM = Zn for **2** and TM = Co for **3**; Ln = Dy **2-3**). Symmetry operations: (i) 2-x, -y, z; (ii) 1-x, -y, z

Compound	**2**	**3**
Ln1⋯TM1	3.3611(8)	3.3545(17)
Ln1⋯Ln1	8.6991(6) (i)	8.750(1) (ii)
TM1⋯TM1	7.6269(9) (i)	7.661(2) (ii)
Ln1-O1	2.286(4)	2.291(9)
Ln1-O2	2.536(5)	2.563(9)
Ln1-O3	2.313(4)	2.322(9)
Ln1-O4	2.653(5)	2.665(9)
Ln1-O7	2.227(4)	2.234(8)
Ln1-O8	2.708(5)	2.710(9)
Ln1-O1N	2.456(5)	2.467(10)
Ln1-O2N	2.519(4)	2.517(10)
Ln1-O1S	2.320(4)	2.321(9)
TM1-N1	2.101(5)	2.111(11)
TM1-N2	2.190(5)	2.196(10)
TM1-O1	2.083(4)	2.079(9)
TM1-O3	1.995(5)	1.965(9)
TM1-O2S	1.979(4)	1.994(9)
Ln1-O1-TM1	100.46(17)	100.2(4)
Ln1-O3-TM1	102.3(2)	102.6(4)
O1-Ln1-O3	65.96(15)	65.8(3)
O1-Ln1-O7	137.32(16)	137.3(3)
O1-Ln1-O1N	83.69(16)	83.1(3)
O1-Ln1-O2N	92.24(15)	92.0(3)
O1-Ln1-O1S	81.44(15)	81.3(3)
O3-Ln1-O7	143.73(15)	144.3(3)
O3-Ln1-O1N	78.55(16)	78.1(3)
O3-Ln1-O2N	127.66(15)	127.6(3)
O3-Ln1-O1S	84.52(16)	84.7(3)
O7-Ln1-O1N	123.75(15)	124.0(3)
O7-Ln1-O2N	84.53(14)	84.2(3)
O7-Ln1-O1S	75.29(14)	75.6(3)
O1-TM1-O3	75.72(17)	76.5(4)
O1-TM1-O2S	96.48(18)	96.3(4)
O3-TM1-O2S	107.65(18)	107.1(4)
N1-TM1-N2	84.3(2)	83.9(4)

S5.- Continuous Shape Measurements (CShM)

Table S6.- Continuous Shape Measurements for the TMN_2O_3 (where TM is Zn or Co) coordination environment in compounds **1**, **2** and **3**.

PP-5	1 D5h	Pentagon
vOC-5	2 C4v	Vacant octahedron
TBPY-5	3 D3h	Trigonal bipyramid
SPY-5	4 C4v	Spherical square pyramid
JTBPY-5	5 D3h	Johnson trigonal bipyramid J12

Structure [ML5]	PP-5	vOC-5	TBPY-5	SPY-5	JTBPY-5
Zn1A (1)	30.823	2.719	4.182	**0.853**	6.711
Zn1B (1)	31.431	2.883	5.082	**0.820**	7.485
Zn1 (2)	29.270	2.116	4.850	**0.724**	6.843
Co1 (3)	29.733	1.975	4.720	**0.747**	6.598

Table S7.- Continuous Shape Measurements for the DyO_9 coordination environment in compounds **1**, **2** and **3**.

EP-9	1 D9h	Enneagon
OPY-9	2 C8v	Octagonal pyramid
HBPY-9	3 D7h	Heptagonal bipyramid
JTC-9	4 C3v	Johnson triangular cupola J3
JCCU-9	5 C4v	Capped cube J8
CCU-9	6 C4v	Spherical-relaxed capped cube
JCSAPR-9	7 C4v	Capped square antiprism J10
CSAPR-9	8 C4v	Spherical capped square antiprism
JTCTPR-9	9 D3h	Tricapped trigonal prism J51
TCTPR-9	10 D3h	Spherical tricapped trigonal prism
JTDIC-9	11 C3v	Tridiminished icosahedron J63
HH-9	12 C2v	Hula-hoop
MFF-9	13 Cs	Muffin

Structure [ML9]	EP-9	OPY-9	HBPY-9	JTC-9	JCCU-9	CCU-9	JCSAPR-9
Dy1A (1)	36.050	23.179	18.395	14.580	10.293	8.501	3.625
Dy1B (1)	36.235	23.443	17.621	14.275	9.804	8.084	3.560
Dy1 (2)	33.637	22.257	16.216	16.204	8.183	7.223	3.641
Dy1 (3)	33.643	22.448	16.181	16.120	8.056	7.164	3.520

Structure [ML9]	CSAPR-9	JTCTPR-9	TCTPR-9	JTDIC-9	HH-9	MFF-9
Dy1A (1)	**2.202**	4.802	2.825	10.230	9.817	2.322
Dy1B (1)	**2.207**	4.328	2.455	10.178	9.531	2.278
Dy1 (2)	3.019	4.137	3.457	11.099	8.242	**2.654**
Dy1 (3)	2.961	4.077	3.433	11.198	8.264	**2.624**

S6.- Additional figures

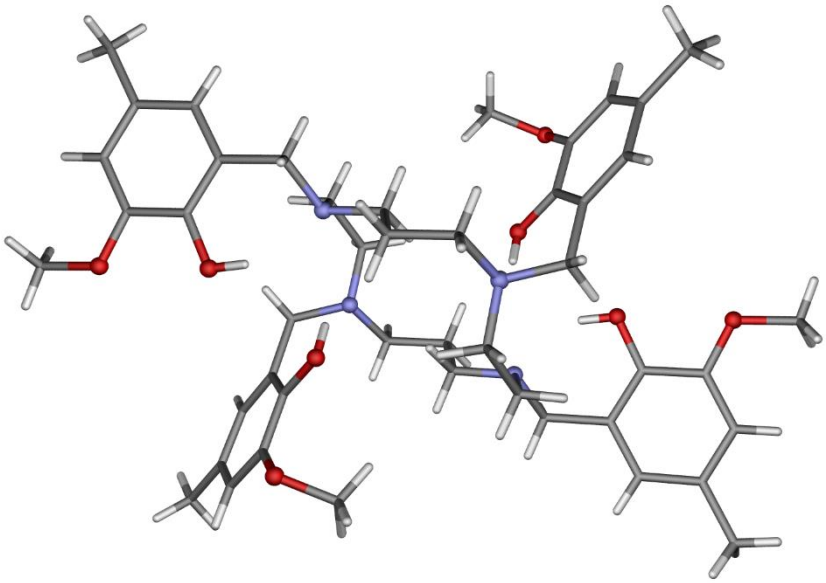

Figure S1.- Perspective view of the structure of H_4L. Oxygen, nitrogen, carbon and hydrogen are in red, blue, grey and white, respectively.

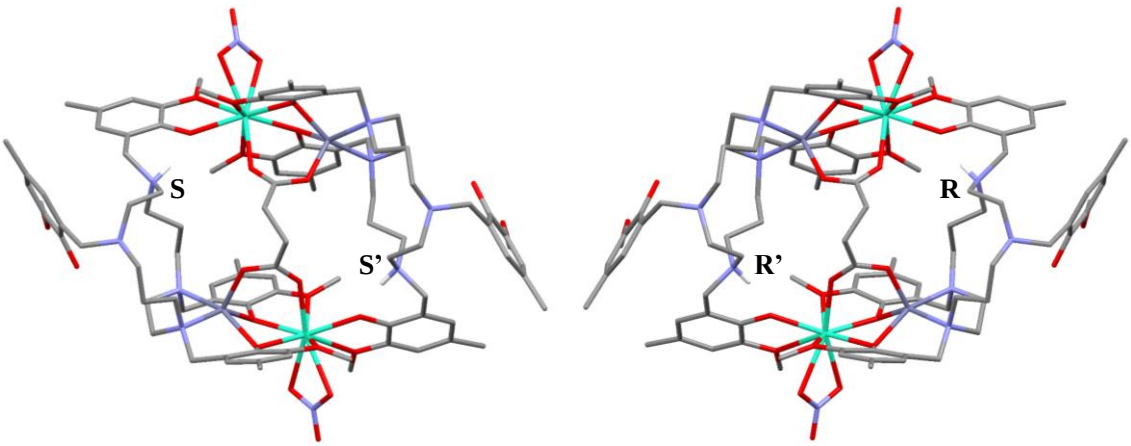

Figure S2.- Perspective view of the two possible enantiomers cocrystallized in **2**. All hydrogen atoms, except the ones that form the asymmetric centers have been omitted for the sake of clarity.

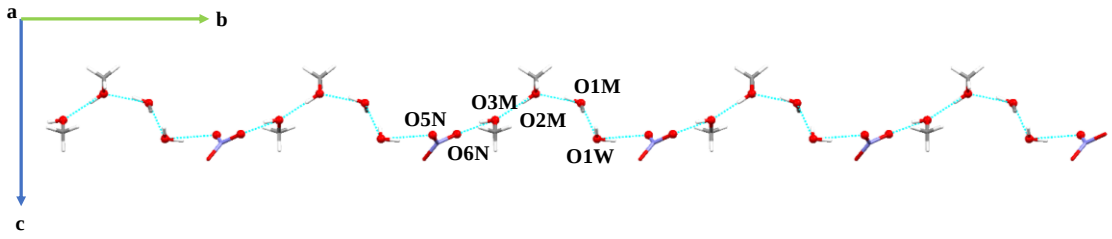

Figure S3.- Hydrogen bonding pattern (blue dashed lines) between counterions (NO_3^-) and solvent molecules (methanol and water) for **3** viewed along the *a* axis. Cationic molecular structures of **3** have been omitted. The methanol related to O1M does not have hydrogen atoms because of the disordered character of the C1M atom.

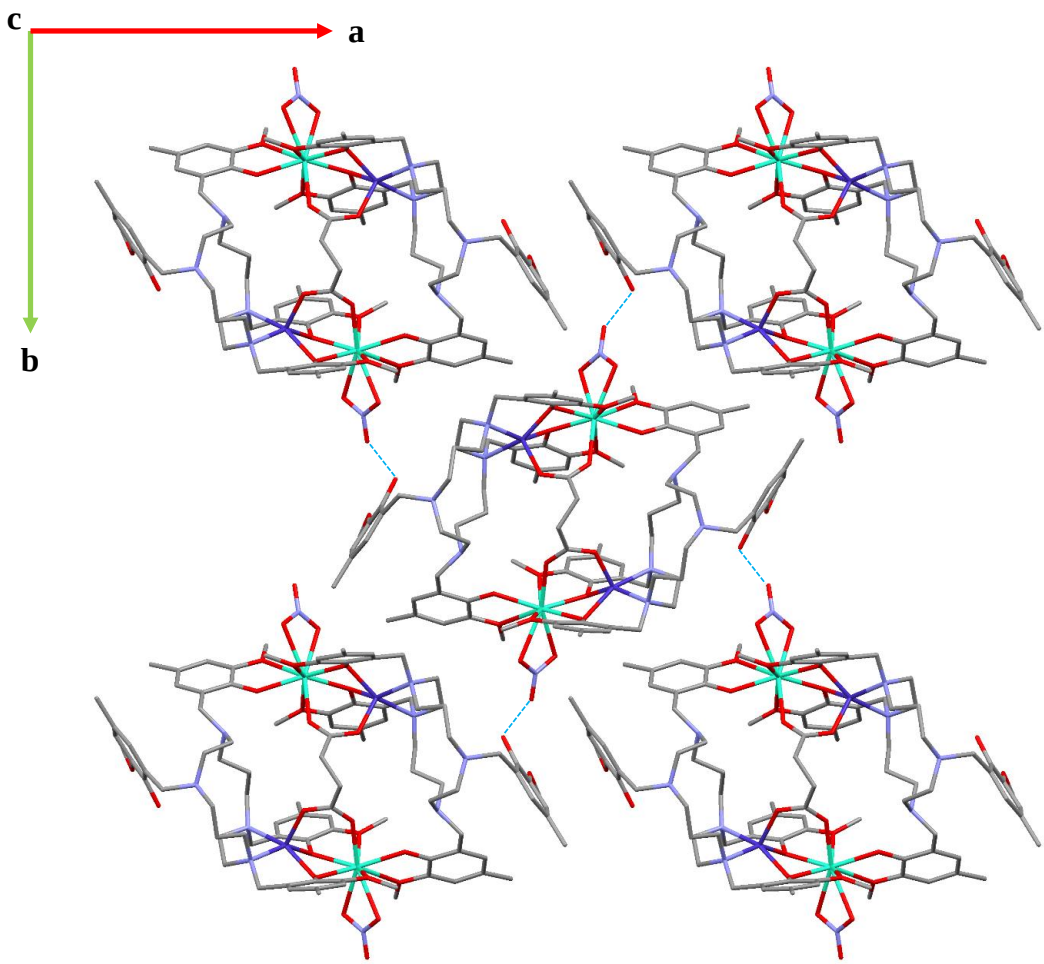

Figure S4.- Hydrogen bonding pattern (blue dashed lines) between cationic fragments of **3**, viewed along the *c* axis. Both possible enantiomers are visible, *R,R'* in the center and *S,S'* in the four vertices.

S7.- Static magnetic properties

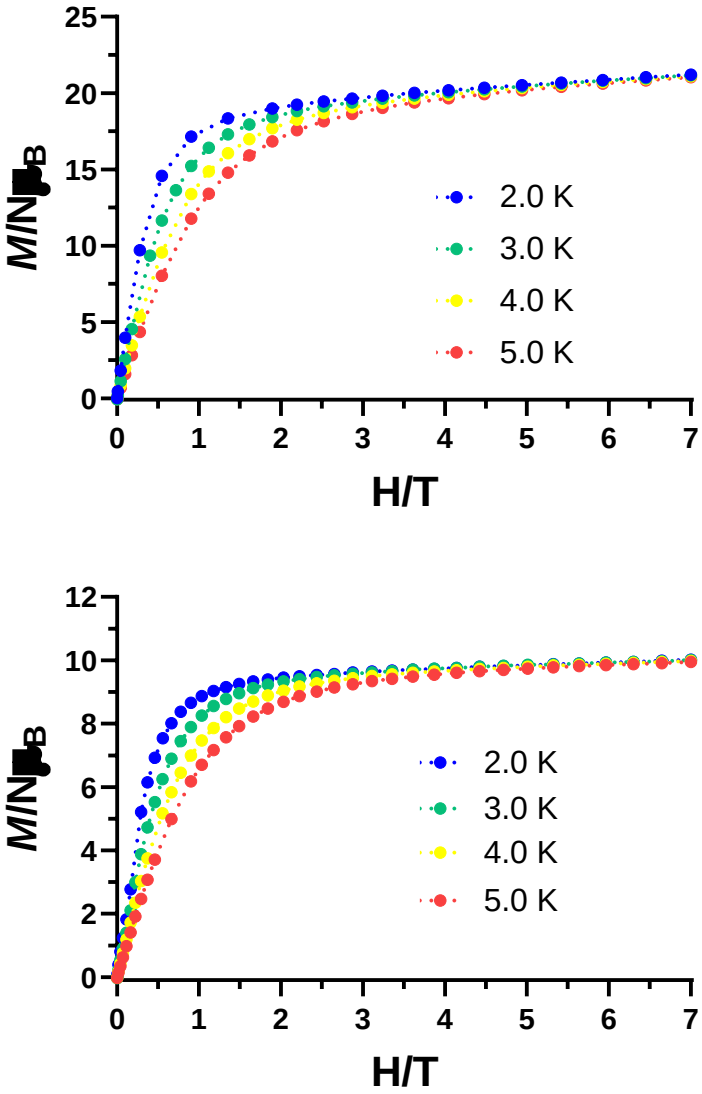

Figure S5.- Magnetization curves in the 2-5 K temperature range for compounds **1** (top) and **2** (bottom). Dashed lines are a guide to the eye.

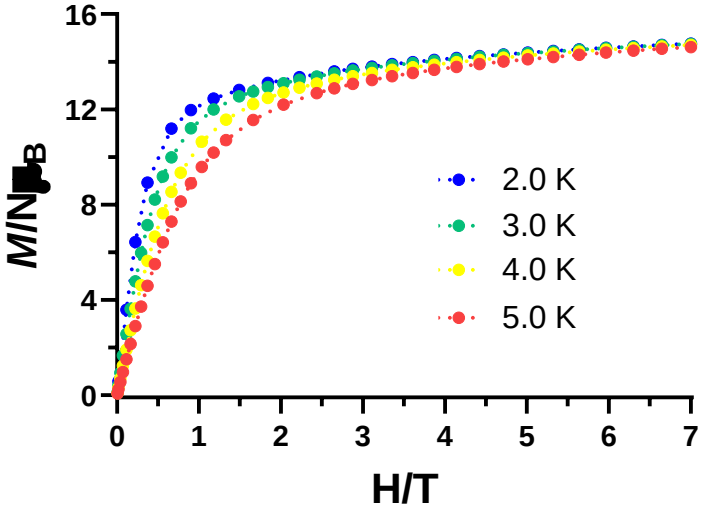

Figure S6.- Magnetization curves in the 2-5 K temperature range for compound **3**. Dashed lines are a guide to the eye.

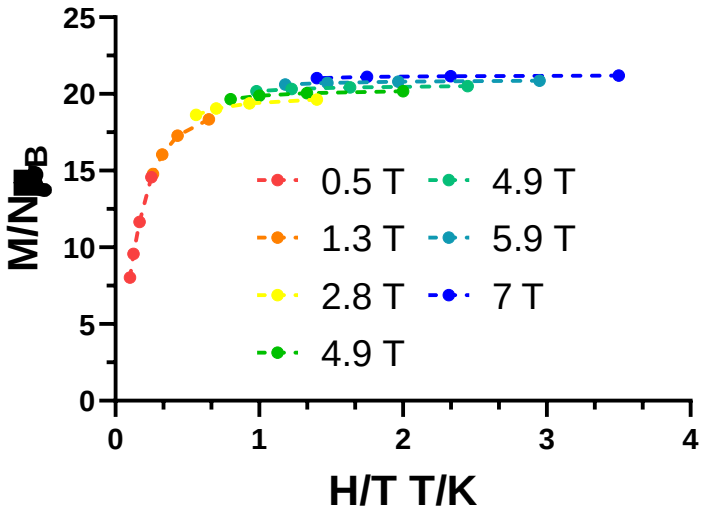

Figure S7.- Isothermal reduced magnetization curves in the 2-5 K temperature range for compound **1**. Dashed lines are a guide to the eye.

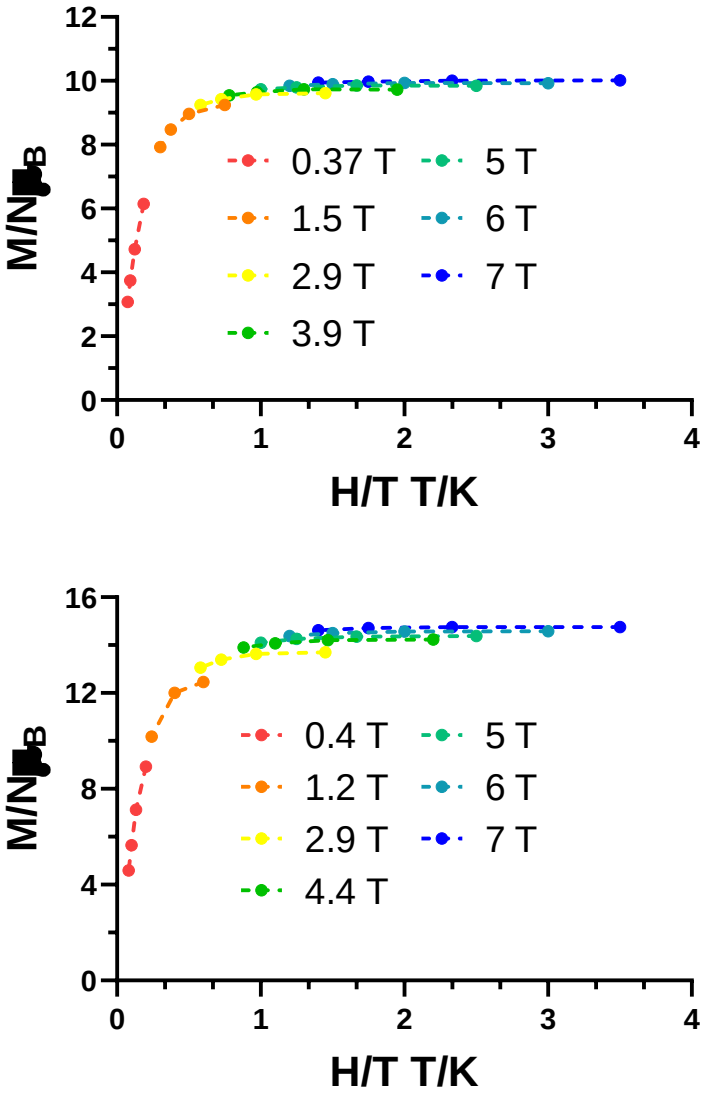

Figure S8.- Isothermal reduced magnetization curves in the 2-5 K temperature range for compounds **2** (top) and **3** (bottom). Dashed lines are a guide to the eye.

S8.- Dynamic magnetic properties

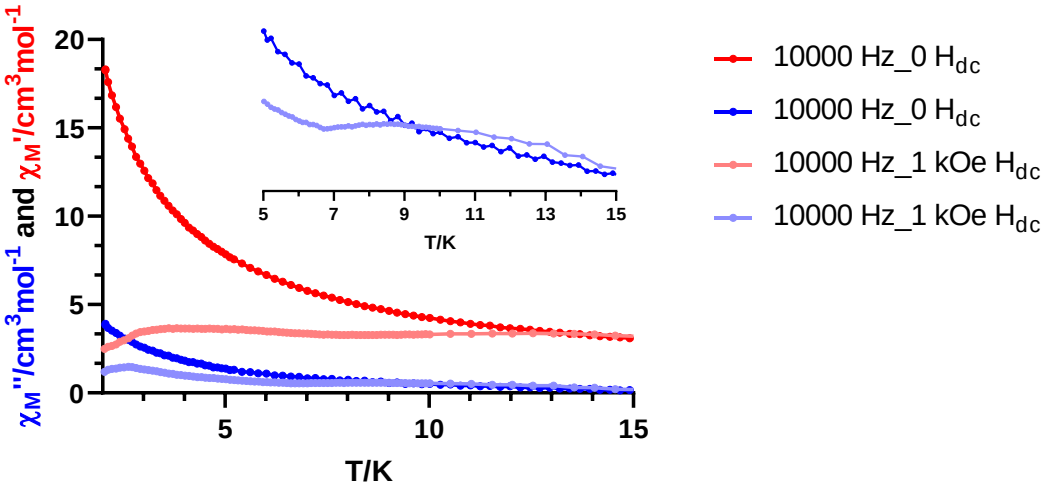

Figure S9.- Temperature dependence of in-phase (red) and out-of-phase (blue) components of the *ac* susceptibility in a zero (dark) and 1 kOe (light) applied *dc* field for **1**.

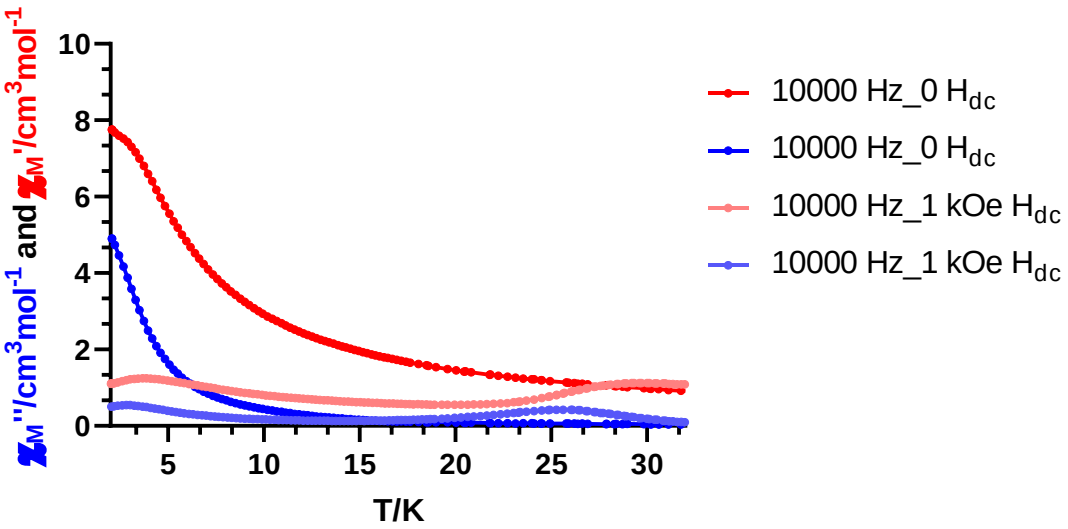

Figure S10.- Temperature dependence of in-phase (red) and out-of-phase (blue) components of the *ac* susceptibility in a zero (dark) and 1 kOe (light) applied *dc* field for **3**.

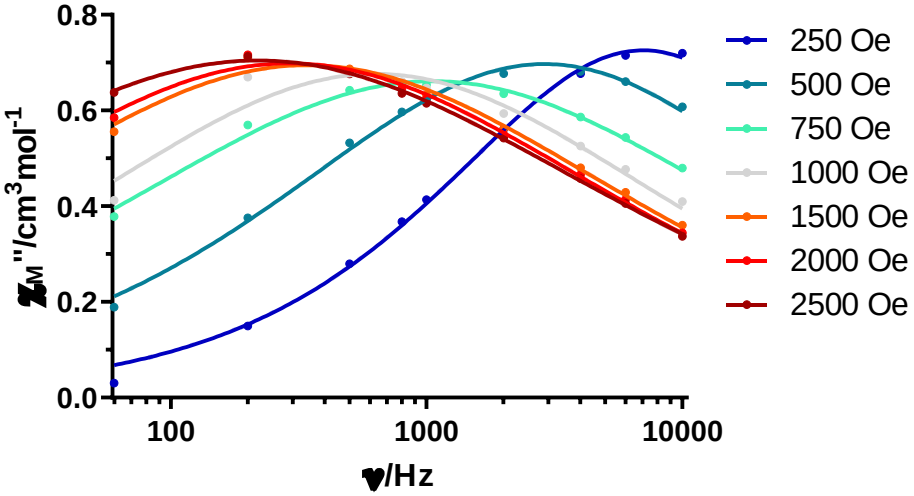

Figure S11.- Field dependence of the out-of-phase signal *vs* frequency at 8.0 K for **1**.

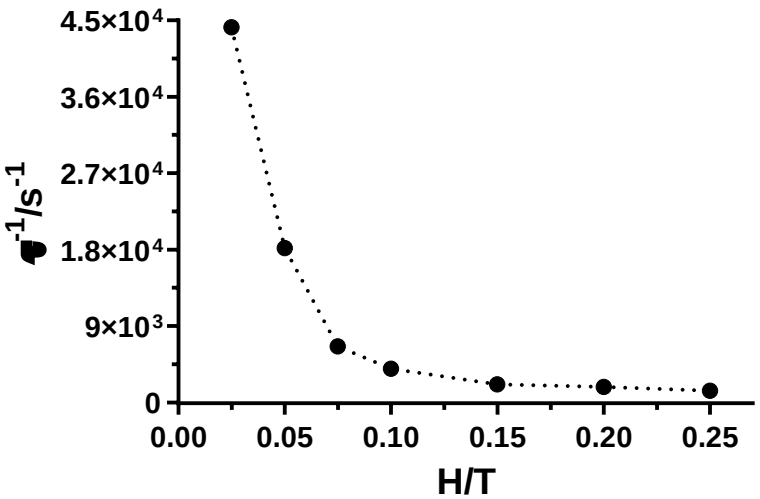

Figure S12.- The inverse of the relaxation times obtained at different magnetic fields at 8.0 K for **1**.

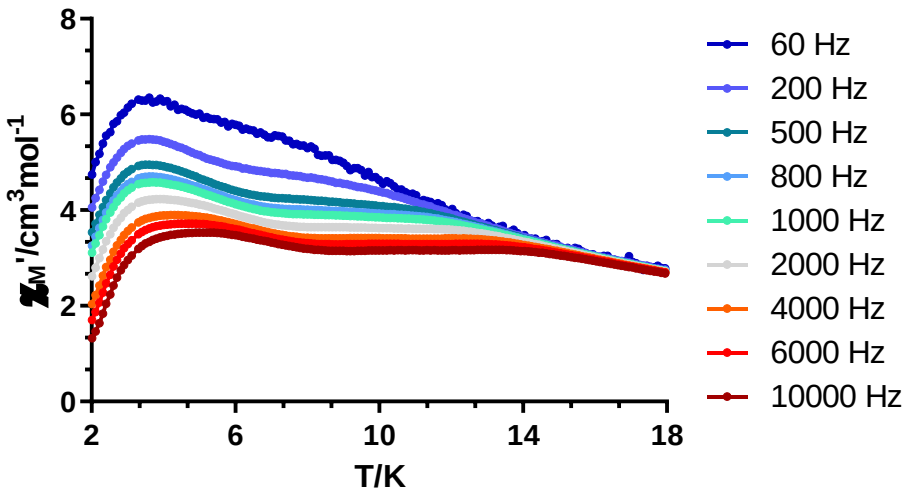

Figure S13.- Temperature dependence of the in phase components of the *ac* susceptibility in a *dc* applied field of 2.5 kOe for **1**.

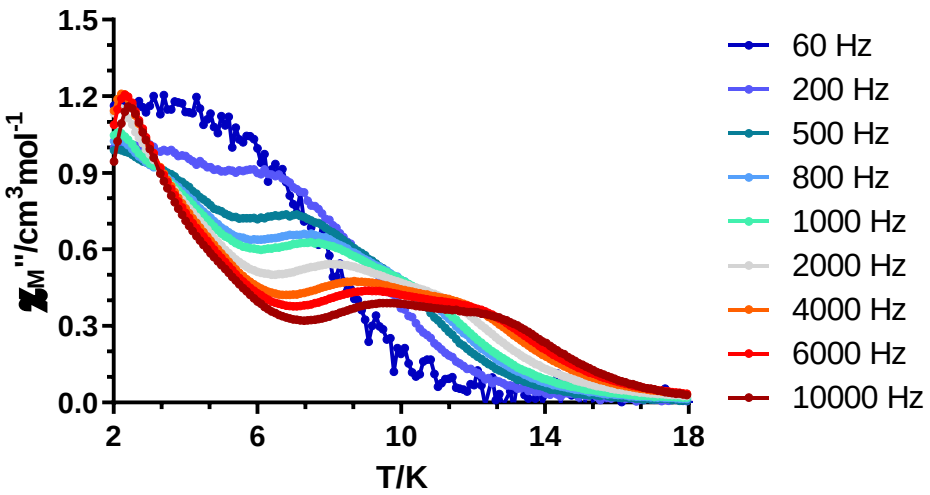

Figure S14.- Temperature dependence of the out-of-phase components of the *ac* susceptibility in a *dc* applied field of 2.5 kOe for **1**.

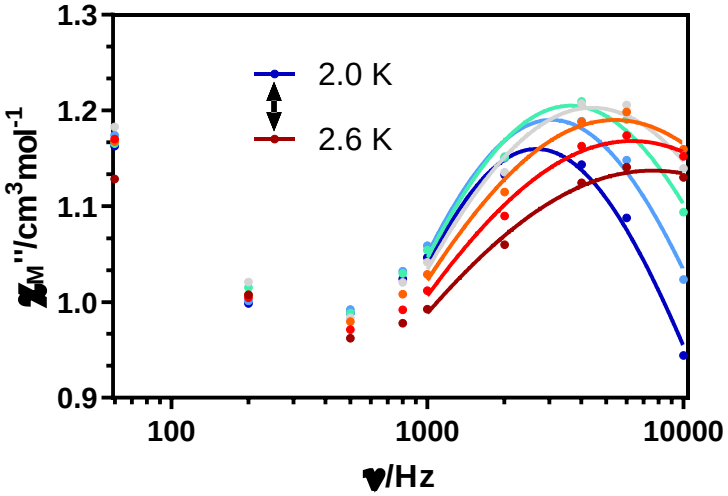

Figure S15.- Variable-temperature frequency dependence of the χ_M'' signal under 2.5 kOe applied field for **1**. Solid lines represent the best fitting of the experimental data to the Debye model.

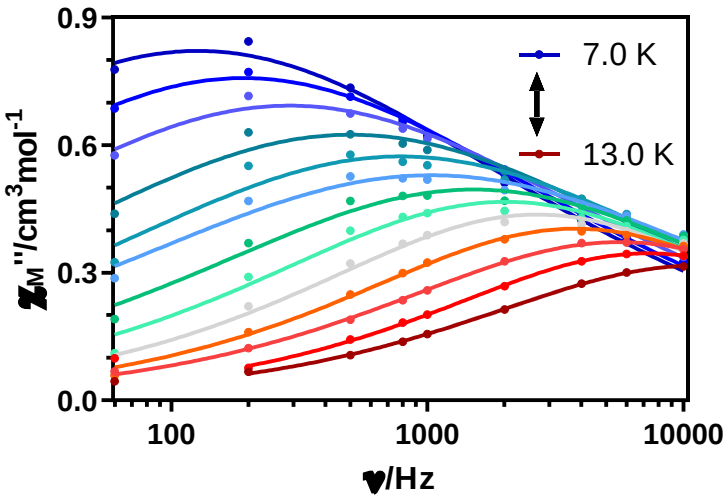

Figure S16.- Variable-temperature frequency dependence of the χ_M'' signal under 2.5 kOe applied field for **1**. Solid lines represent the best fitting of the experimental data to the Debye model.

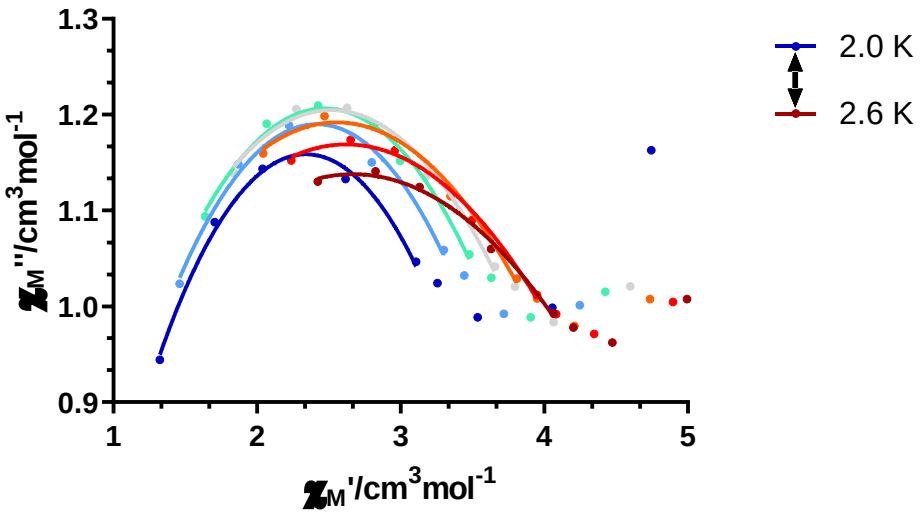

Figure S17.- Cole-Cole plots under 2.5 kOe field for **1**. Solid lines represent the best fit to the generalized Debye model.

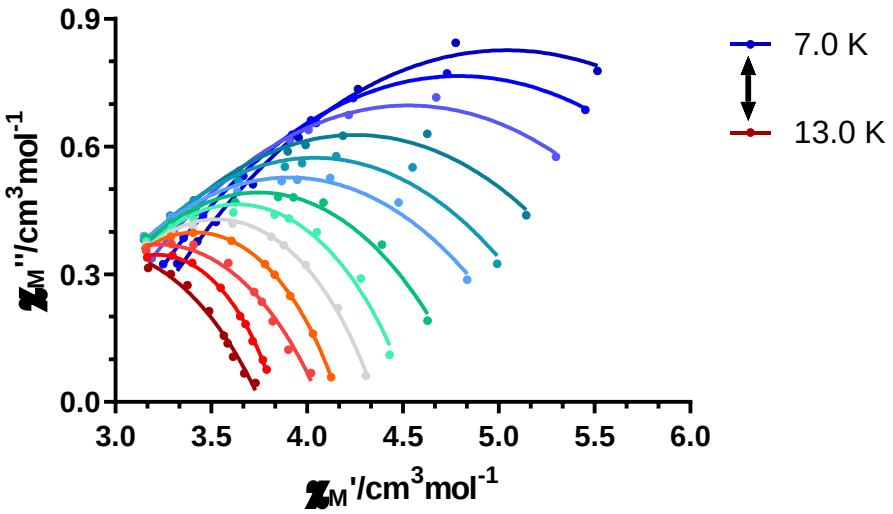

Figure S18.- Cole-Cole plots under 2.5 kOe field for **1**. Solid lines represent the best fit to the generalized Debye model.

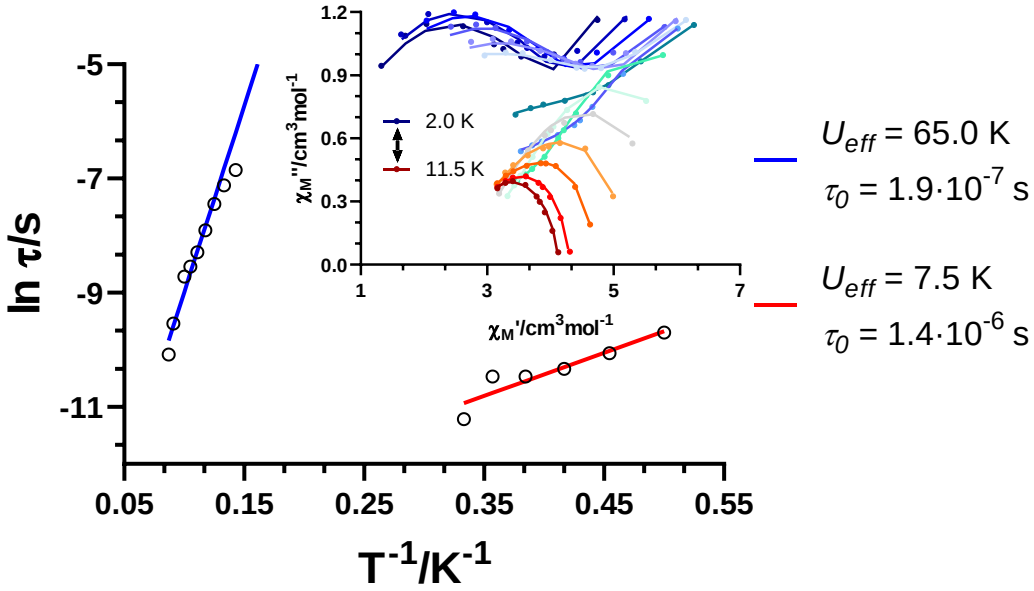

Figure S19.- Arrhenius plot for the relaxation times with Orbach fittings for FR and SR. Inset: Cole-Cole plots under 2.5 kOe field for **1**. Solid lines represent the best fit using a sum of two modified Debye functions.

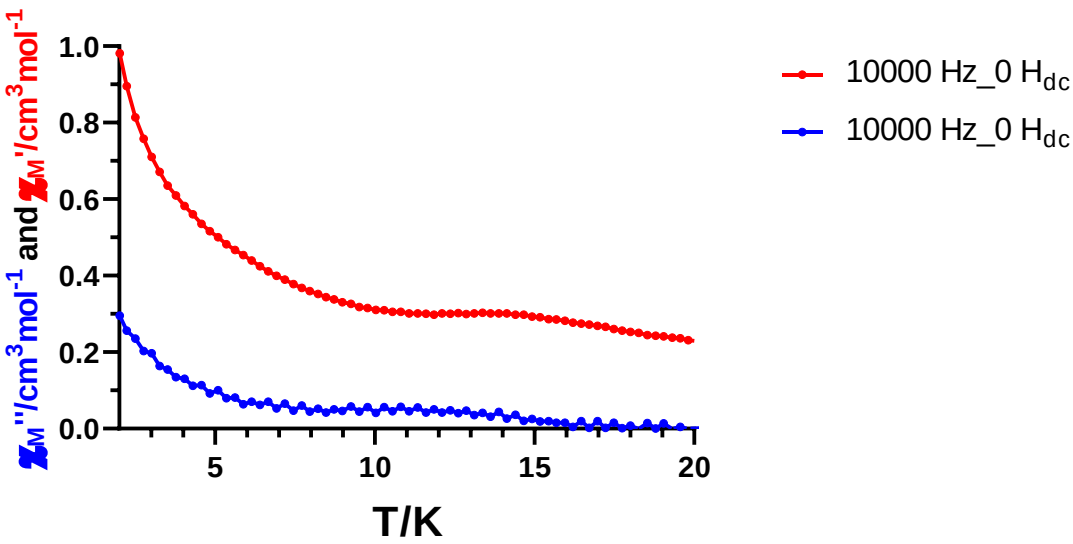

Figure S20.- Temperature dependence of in-phase (red) and out-of-phase (blue) components of the *ac* susceptibility in a zero applied *dc* field for **1Y**.

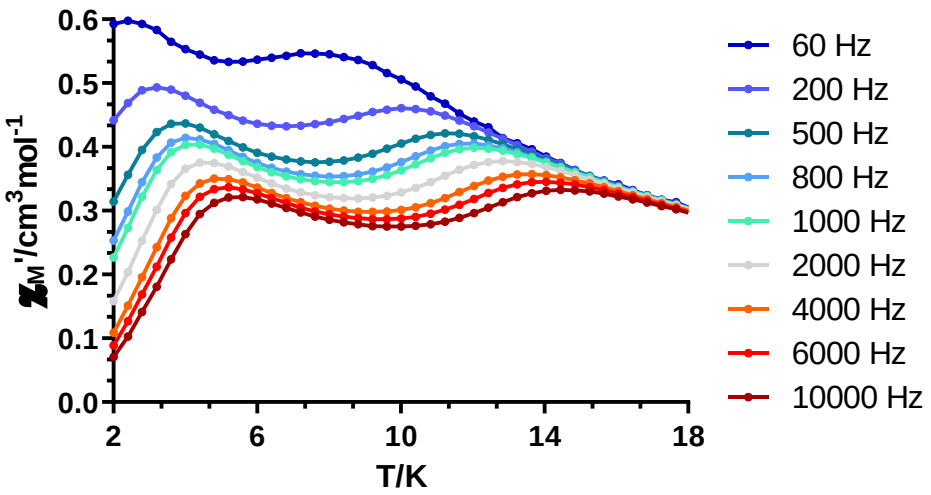

Figure S21.- Temperature dependence of the in phase components of the *ac* susceptibility in a *dc* applied field of 2.5 kOe for **1**$_{\mathbf{Y}}$.

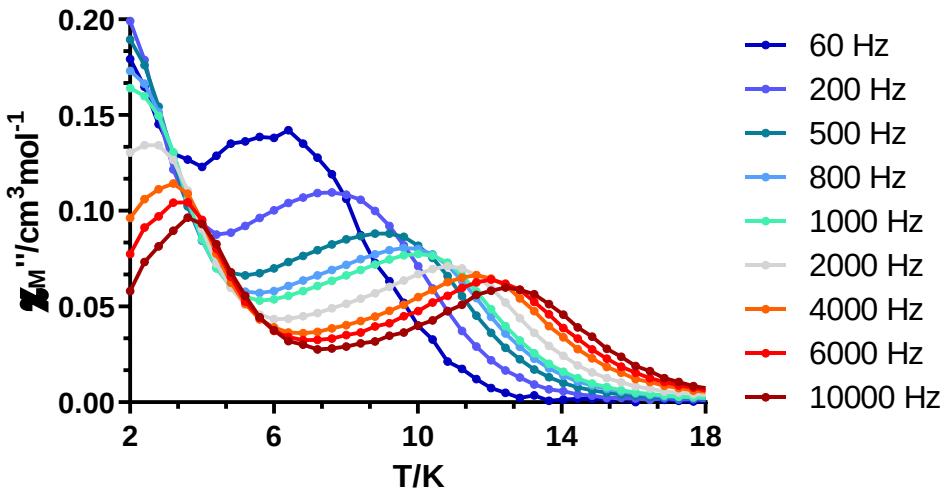

Figure S22.- Temperature dependence of the out-of-phase components of the *ac* susceptibility in a *dc* applied field of 2.5 kOe for **1**$_{\mathbf{Y}}$.

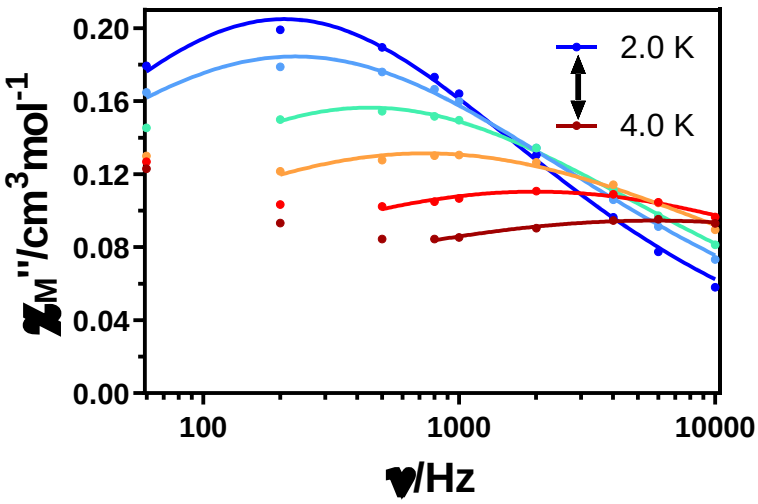

Figure S23.- Variable-temperature frequency dependence of the χ_M'' signal under 2.5 kOe applied field for **1**$_Y$. Solid lines represent the best fitting of the experimental data to the Debye model.

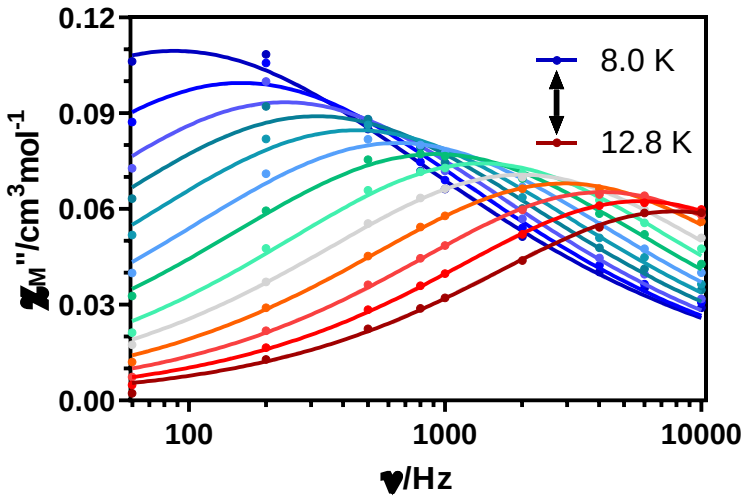

Figure S24.- Variable-temperature frequency dependence of the χ_M'' signal under 2.5 kOe applied field for **1**$_Y$. Solid lines represent the best fitting of the experimental data to the Debye model.

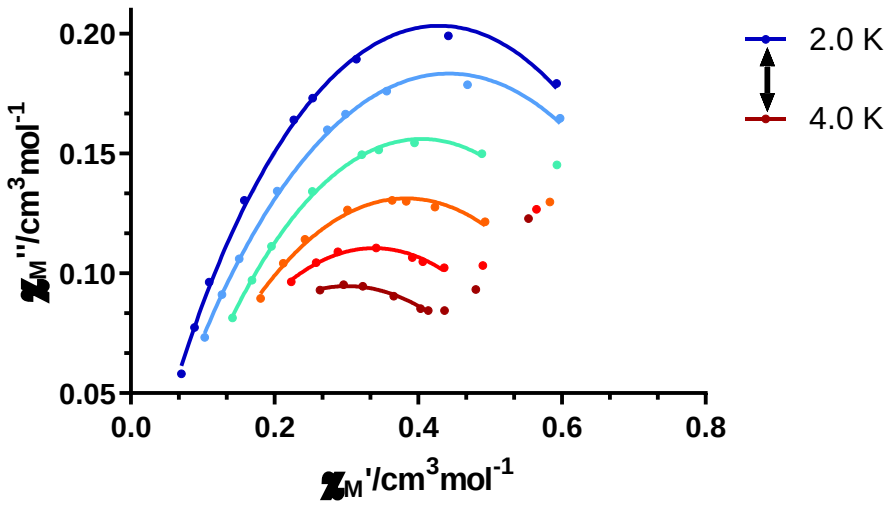

Figure S25.- Cole-Cole plots under 2.5 kOe field for **1Y**. Solid lines represent the best fit to the generalized Debye model.

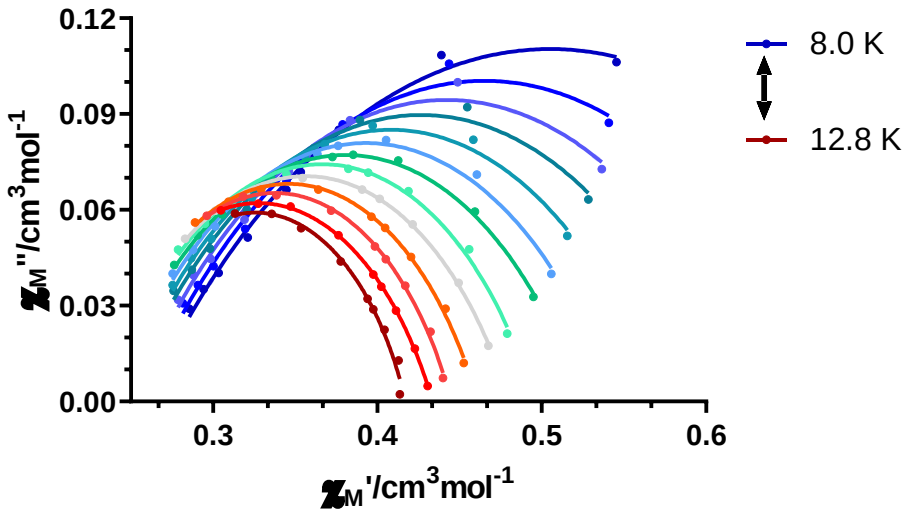

Figure S26.- Cole-Cole plots under 2.5 kOe field for **1Y**. Solid lines represent the best fit to the generalized Debye model.

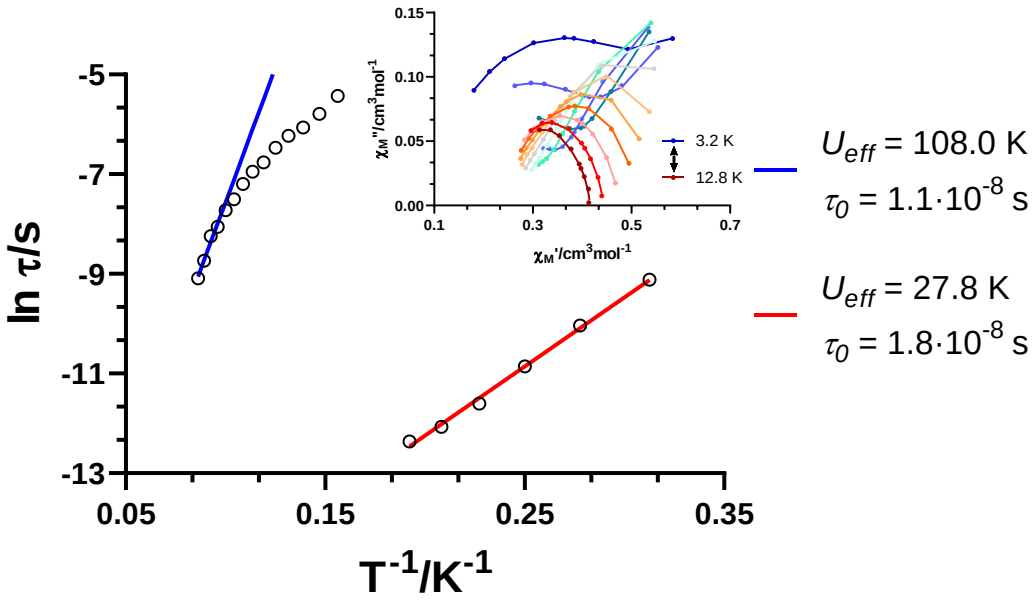

Figure S27.- Arrhenius plot for the relaxation times with Orbach fittings for FR and SR. Inset: Cole-Cole plots under 2.5 kOe field for **1Y**. Solid lines represent the best fit using a sum of two modified Debye functions.

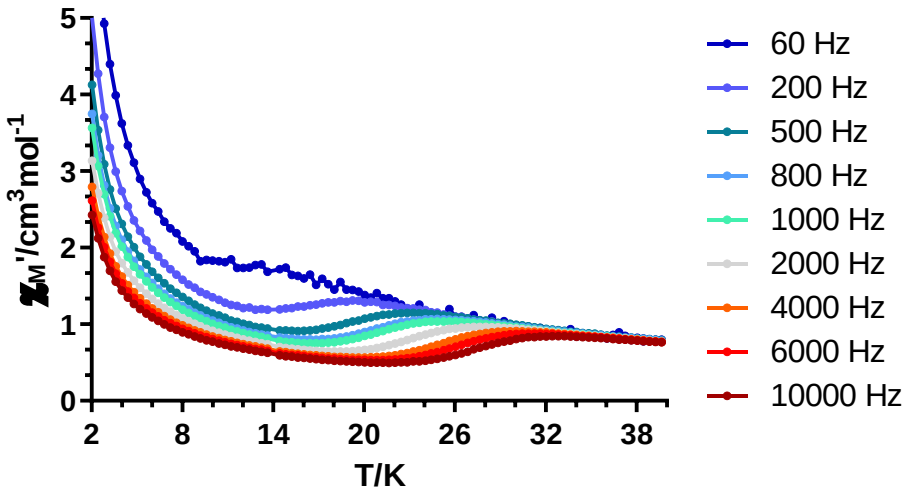

Figure S28.- Temperature dependence of the in phase components of the *ac* susceptibility in a zero applied field for **2**.

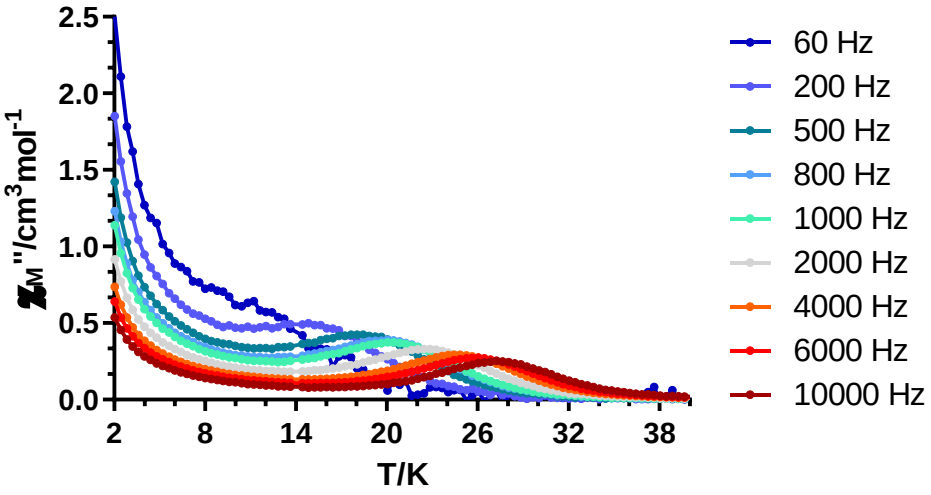

Figure S29.- Temperature dependence of the out-of-phase components of the *ac* susceptibility in a zero applied field for **2**.

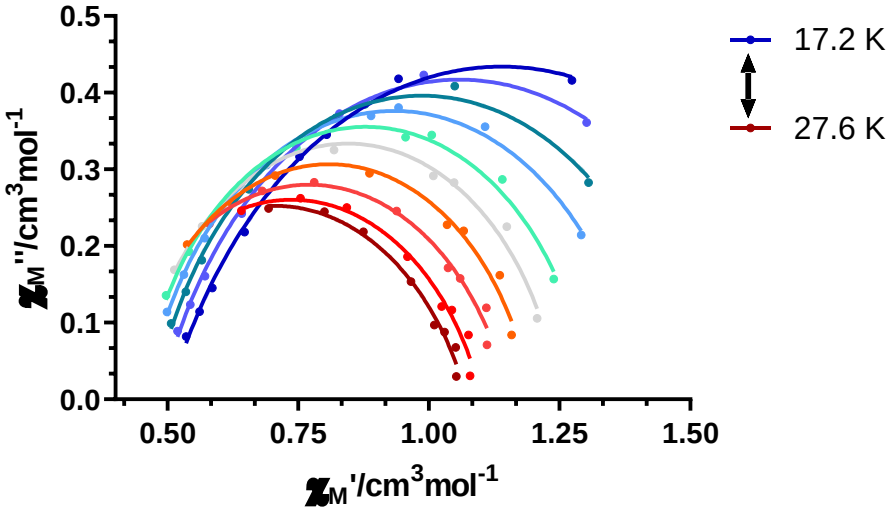

Figure S30.- Cole-Cole plots under zero field for **2**. Solid lines represent the best fit to the generalized Debye model.

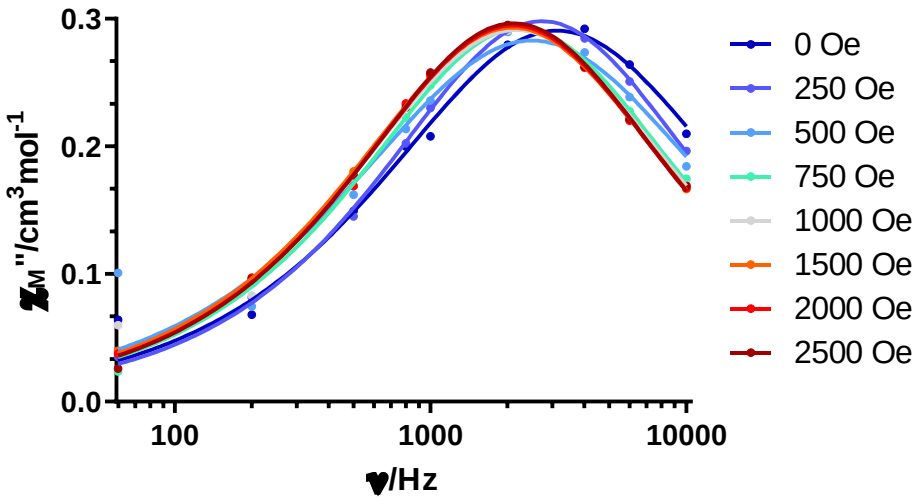

Figure S31.- Field dependence of the out-of-phase signal *vs* frequency at 24.8 K for **2**.

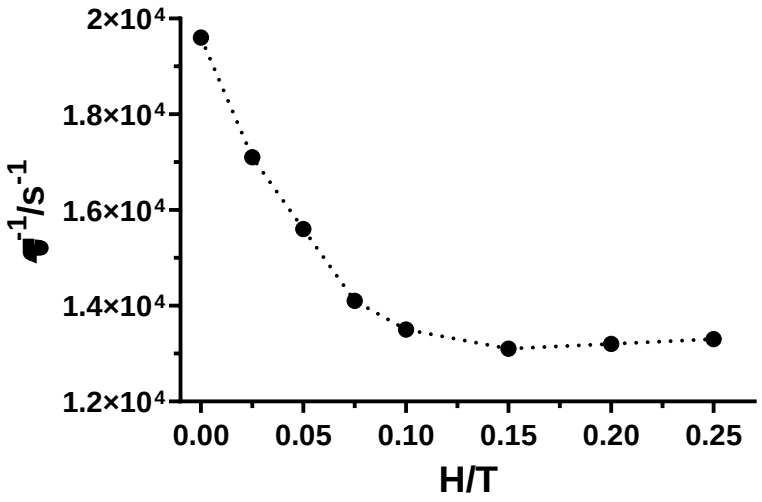

Figure S32.- The inverse of the relaxation times obtained at different magnetic fields at 24.8 K for **2**.

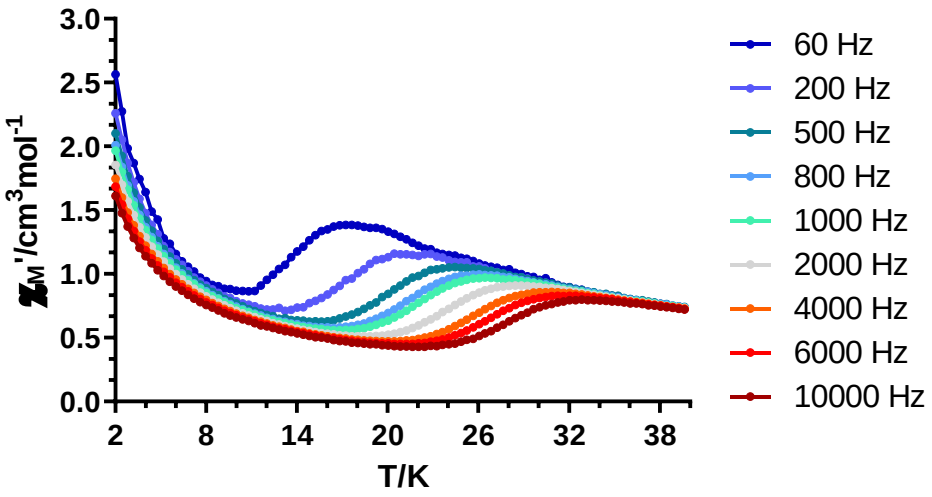

Figure S33.- Temperature dependence of the in phase components of the *ac* susceptibility in a *dc* applied field of 1 kOe for **2**.

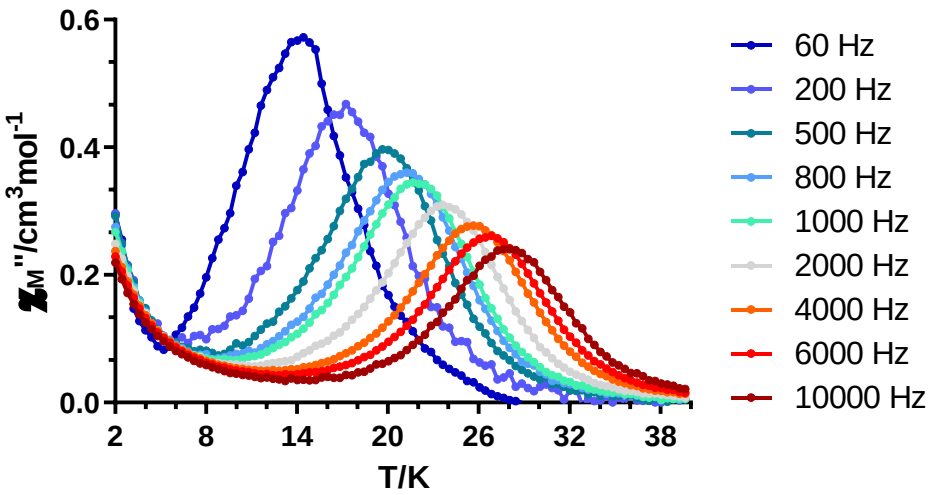

Figure S34.- Temperature dependence of the out-of-phase components of the *ac* susceptibility in a *dc* applied field of 1 kOe for **2**.

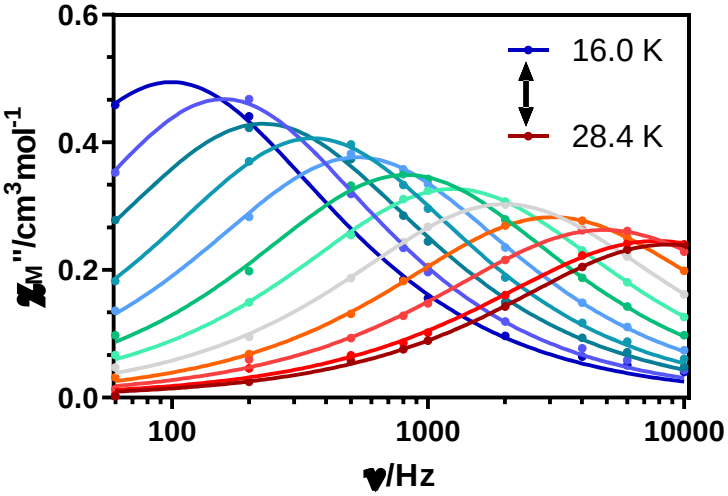

Figure S35.- Variable-temperature frequency dependence of the χ_M'' signal under 1 kOe applied field for **2**. Solid lines represent the best fitting of the experimental data to the Debye model.

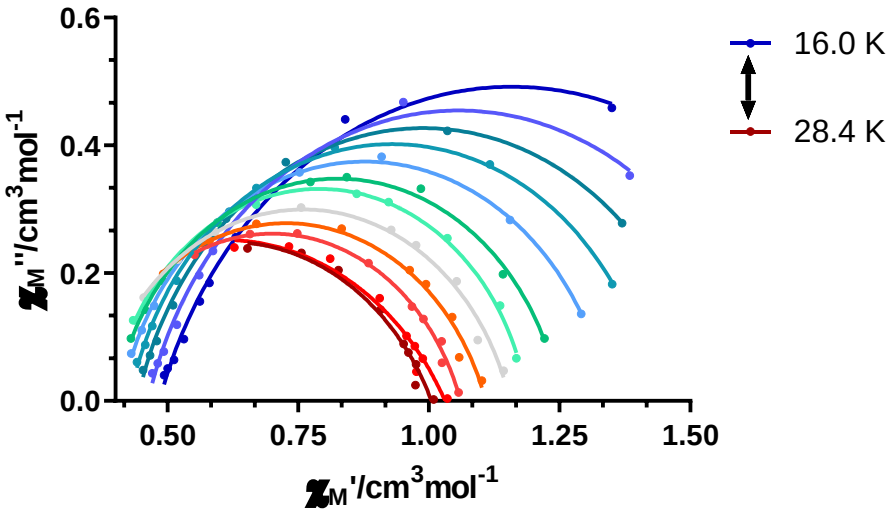

Figure S36.- Cole-Cole plots under 1 kOe field for **2**. Solid lines represent the best fit to the generalized Debye model.

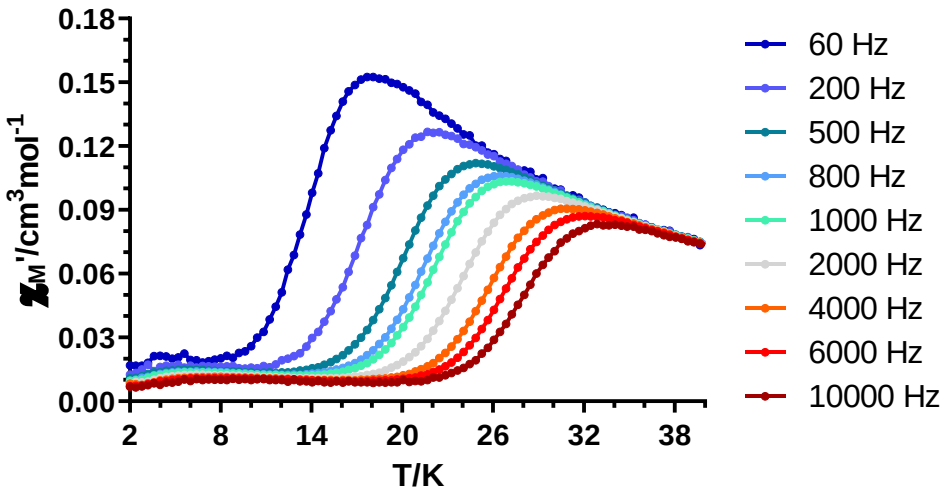

Figure S37.- Temperature dependence of the in phase components of the *ac* susceptibility in a *dc* applied field of 1 kOe for **2Y**.

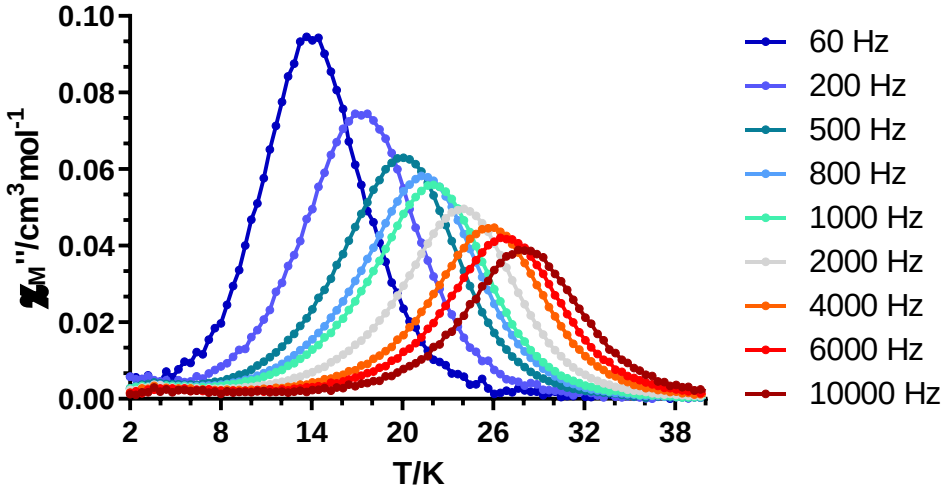

Figure S38.- Temperature dependence of the out-of-phase components of the *ac* susceptibility in a *dc* applied field of 1 kOe for **2Y**.

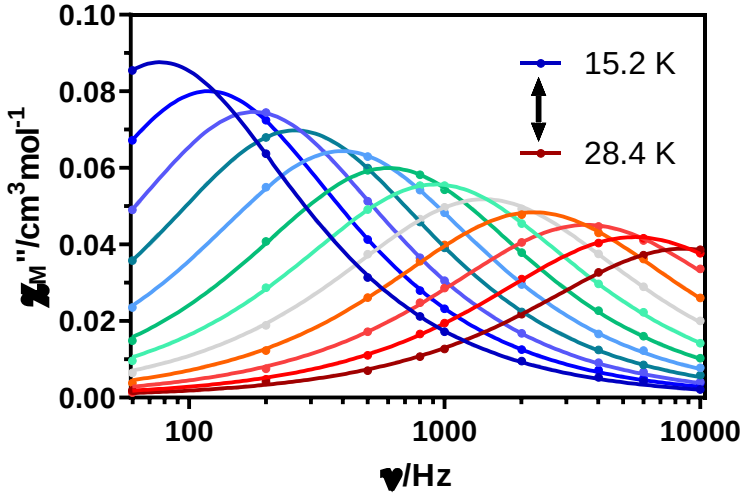

Figure S39.- Variable-temperature frequency dependence of the χ_M'' signal under 1 kOe applied field for **2Y**. Solid lines represent the best fitting of the experimental data to the Debye model.

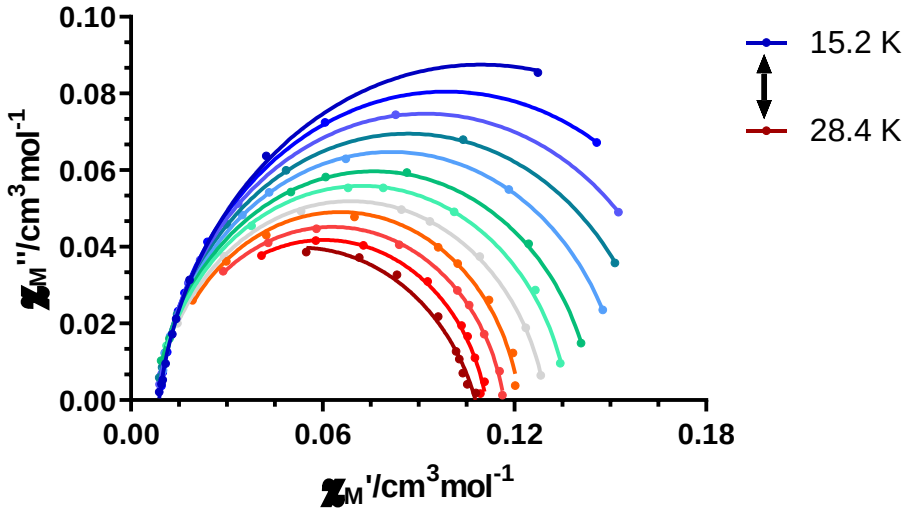

Figure S40.- Cole-Cole plots under 1 kOe field for **2Y**. Solid lines represent the best fit to the generalized Debye model.

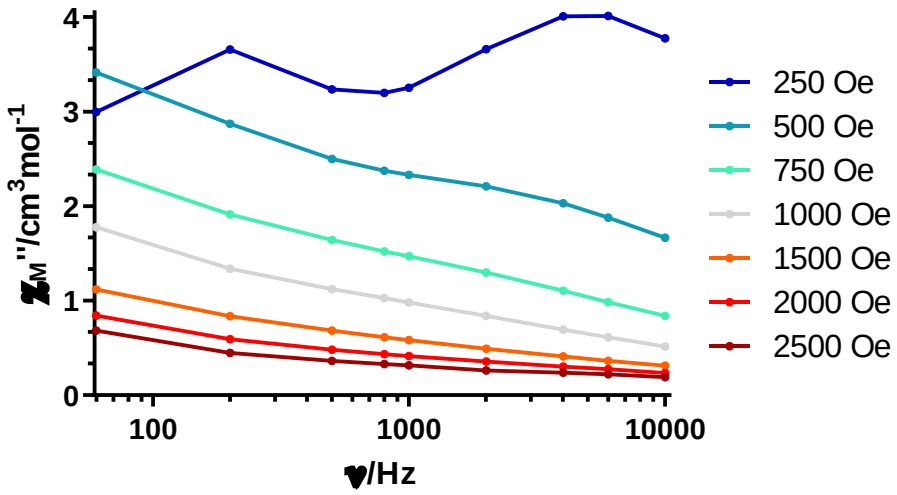

Figure S41.- Field dependence of the out-of-phase signal *vs* frequency at 2.0 K for **3**.

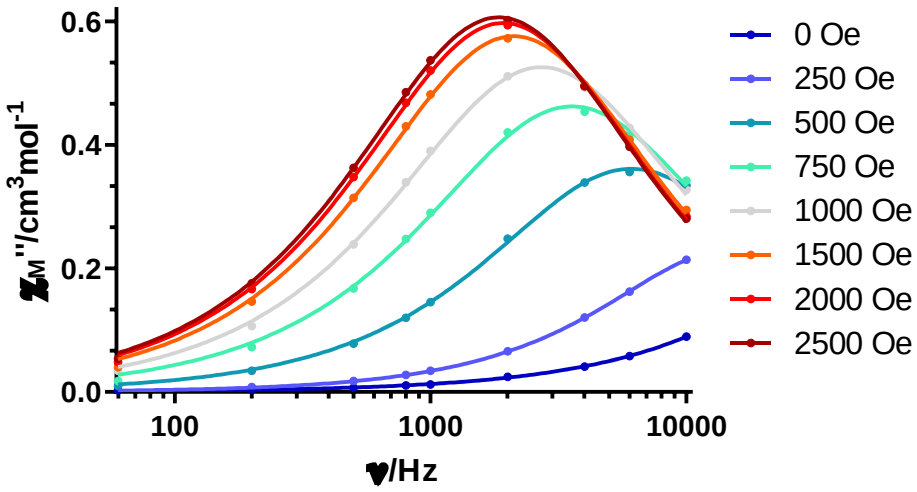

Figure S42.- Field dependence of the out-of-phase signal *vs* frequency at 22.6 K for **3**.

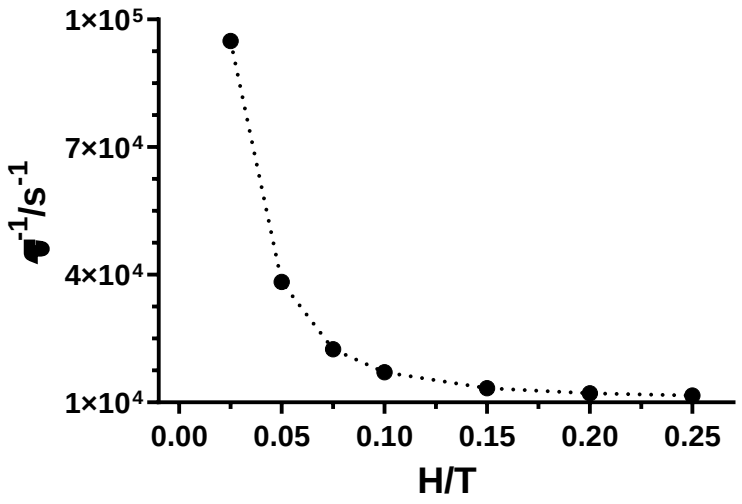

Figure S43.- The inverse of the relaxation times obtained at different magnetic fields at 22.6 K for **3**.

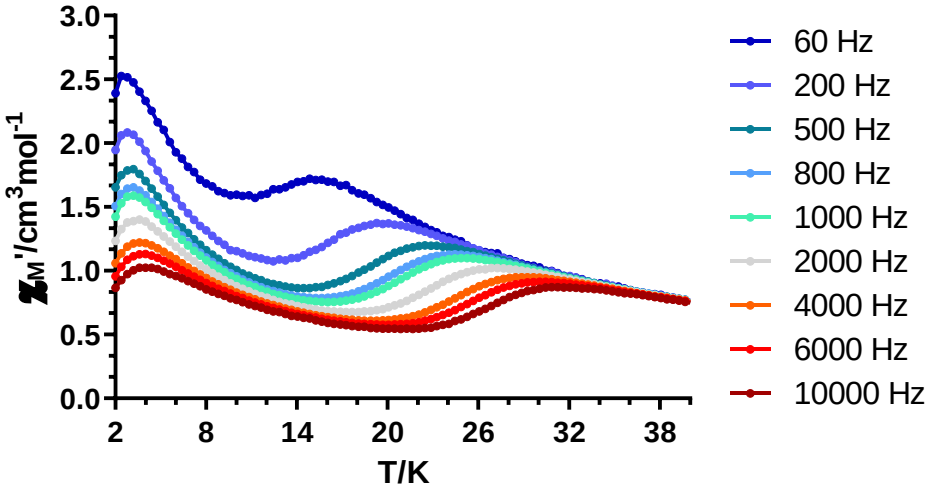

Figure S44.- Temperature dependence of the in phase components of the *ac* susceptibility in a *dc* applied field of 2.5 kOe for **3**.

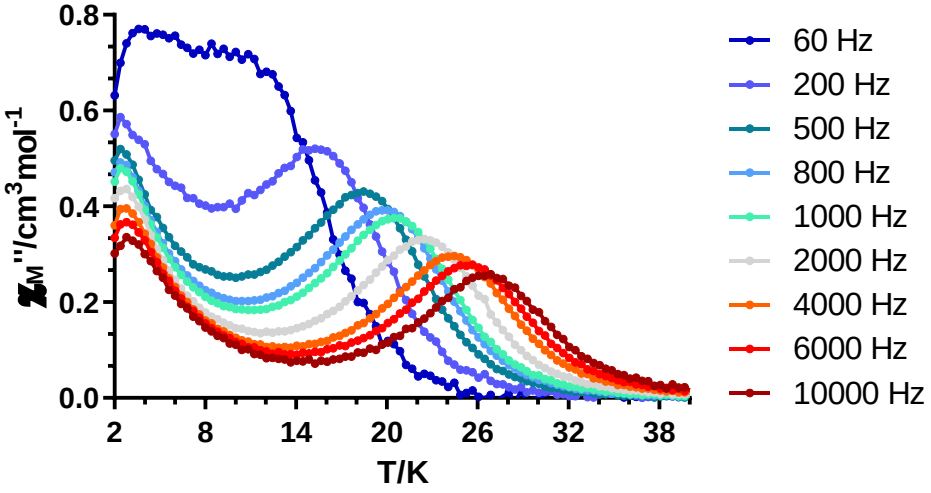

Figure S45.- Temperature dependence of the out-of-phase components of the *ac* susceptibility in a *dc* applied field of 2.5 kOe for **3**.

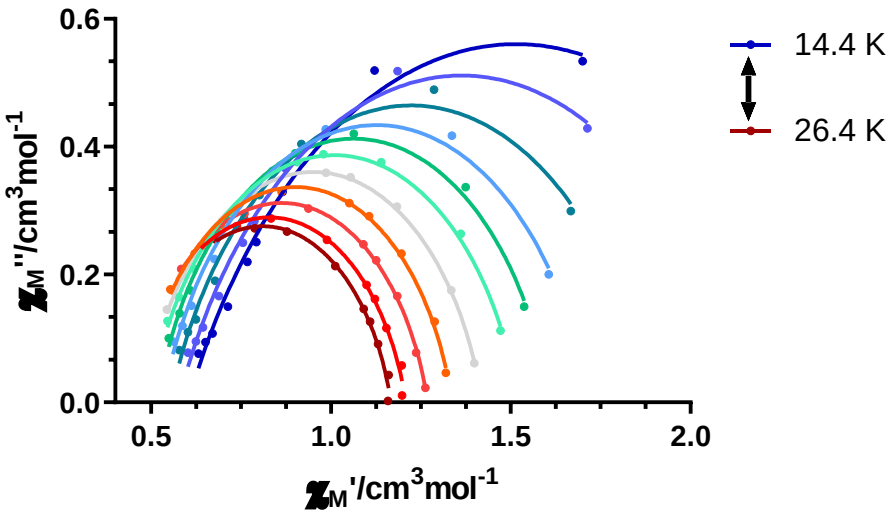

Figure S46.- Cole-Cole plots under 2.5 kOe field for **3**. Solid lines represent the best fit to the generalized Debye model.

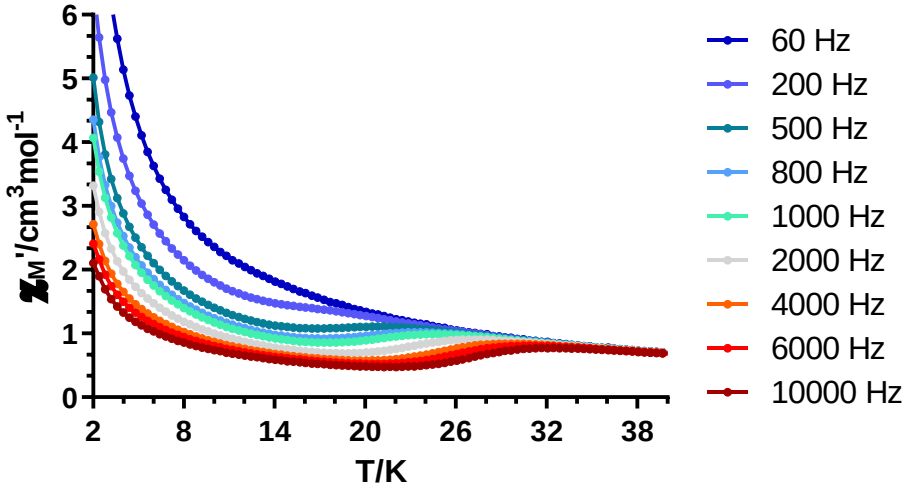

Figure S47.- Temperature dependence of the in phase components of the *ac* susceptibility in a zero applied field for **3Zn**.

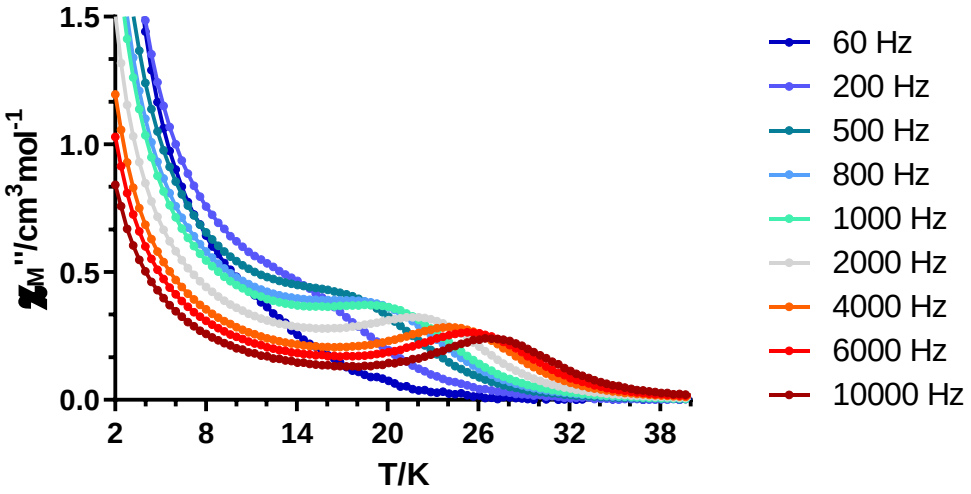

Figure S48.- Temperature dependence of the out-of-phase components of the *ac* susceptibility in a zero applied field for **3Zn**.

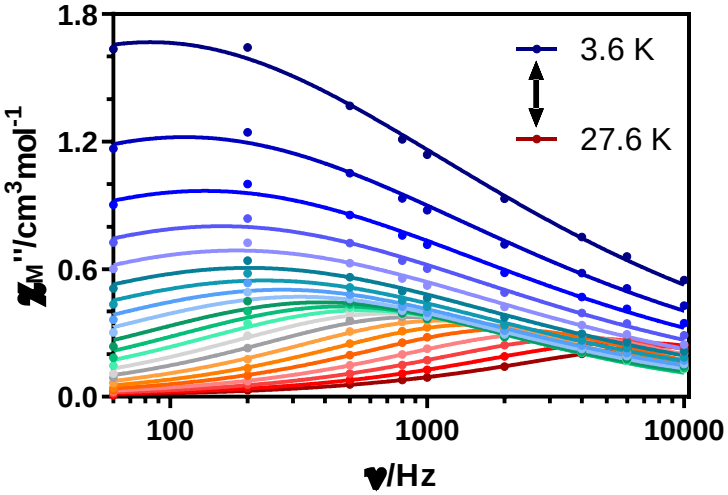

Figure S49.- Variable-temperature frequency dependence of the χ_M'' signal under zero applied field for **3Zn**. Solid lines represent the best fitting of the experimental data to the Debye model.

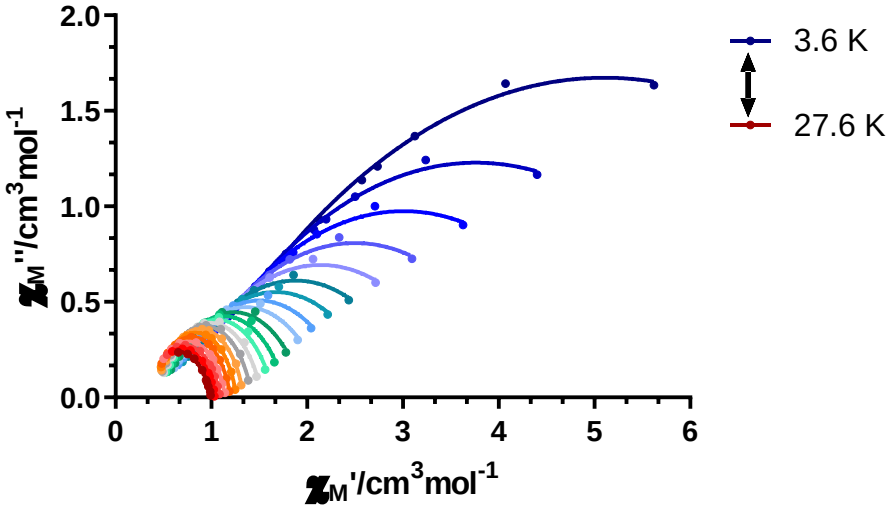

Figure S50.- Cole-Cole plots under zero field for **3Zn**. Solid lines represent the best fit to the generalized Debye model.

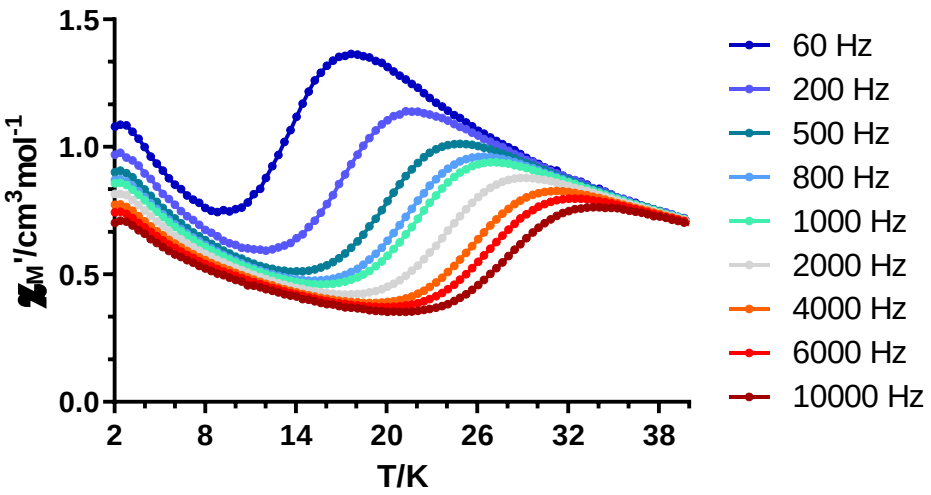

Figure S51.- Temperature dependence of the in phase components of the *ac* susceptibility in a *dc* applied field of 2.5 kOe for **3Zn**.

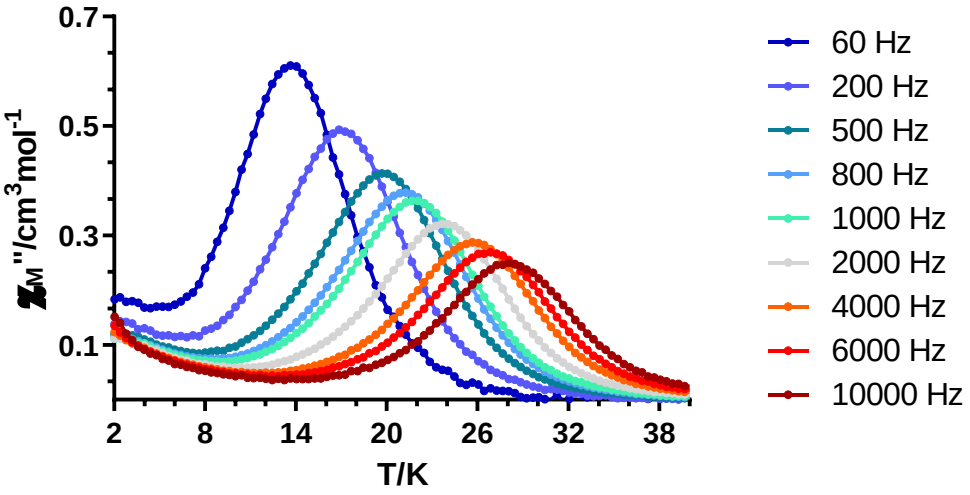

Figure S52.- Temperature dependence of the out-of-phase components of the *ac* susceptibility in a *dc* applied field of 2.5 kOe for **3Zn**.

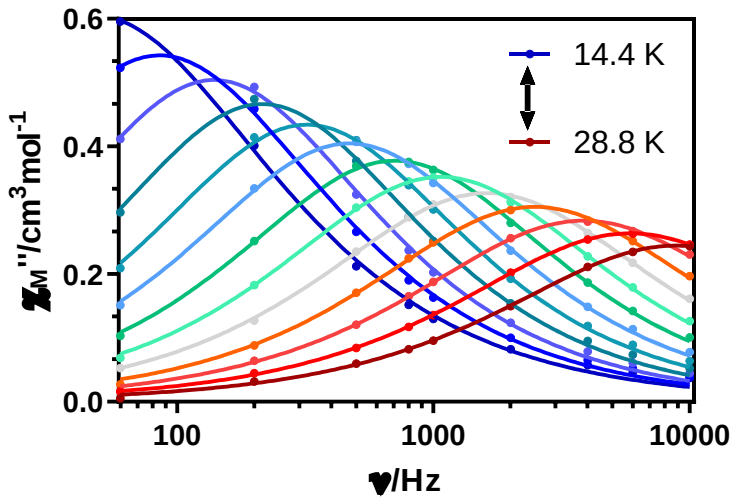

Figure S53.- Variable-temperature frequency dependence of the χ_M'' signal under 2.5 kOe applied field for **3Zn**. Solid lines represent the best fitting of the experimental data to the Debye model.

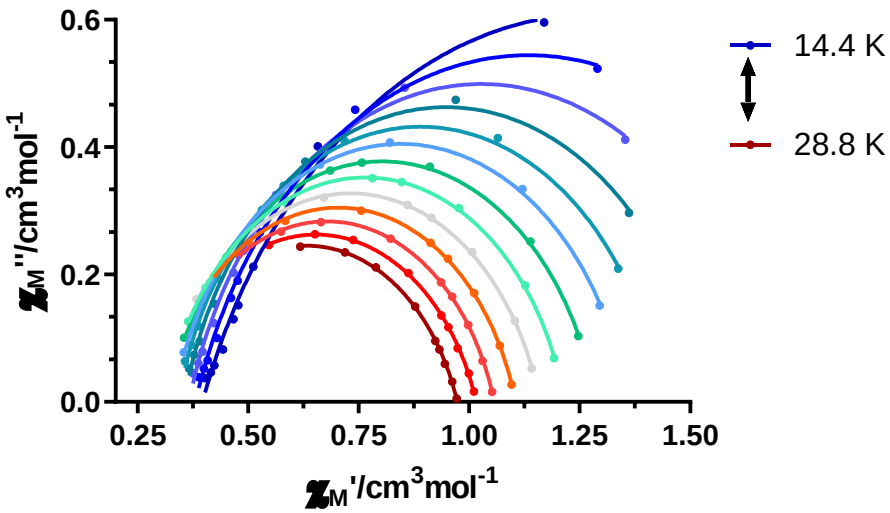

Figure S54.- Cole-Cole plots under 2.5 kOe field for **3Zn**. Solid lines represent the best fit to the generalized Debye model.

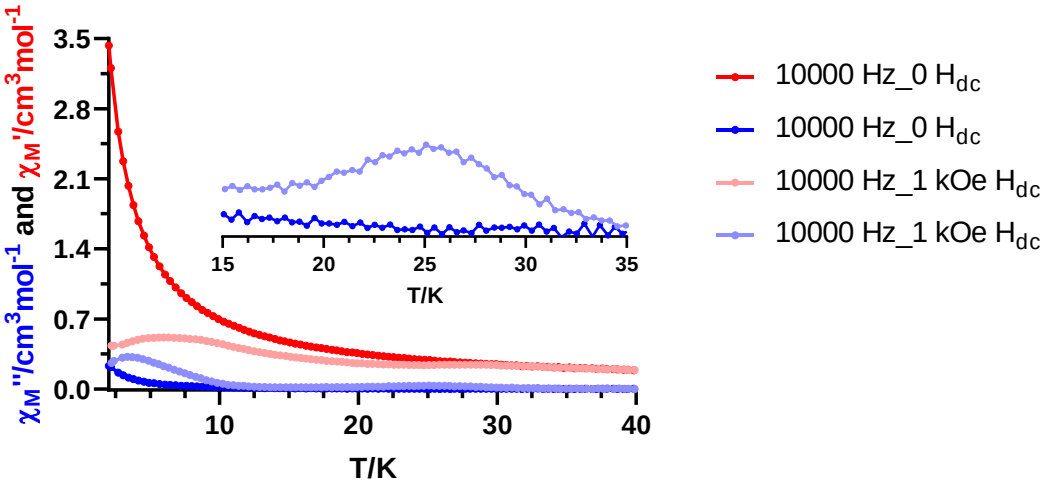

Figure S55.- Temperature dependence of in-phase (red) and out-of-phase (blue) components of the *ac* susceptibility in a zero (dark) and 1 kOe (light) applied *dc* field for **3Y**.

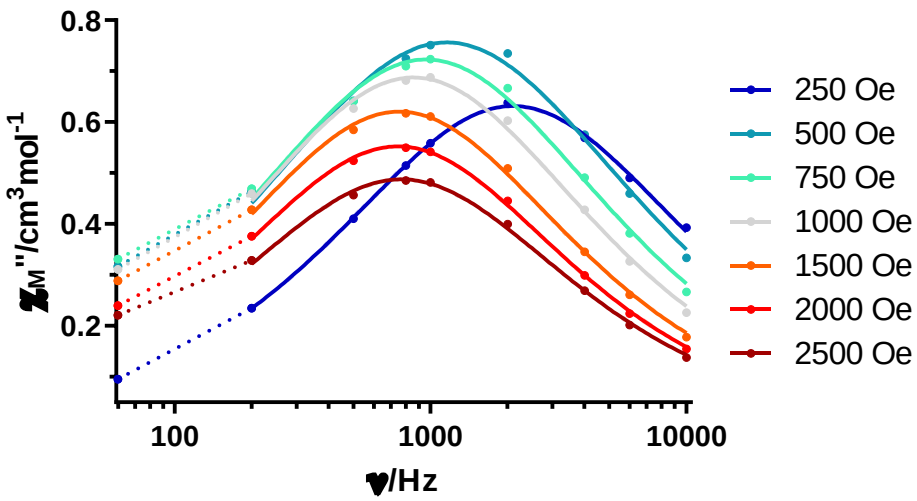

Figure S56.- Field dependence of the out-of-phase signal *vs* frequency at 2.0 K for **3Y**. Dashed lines are a guide to the eye.

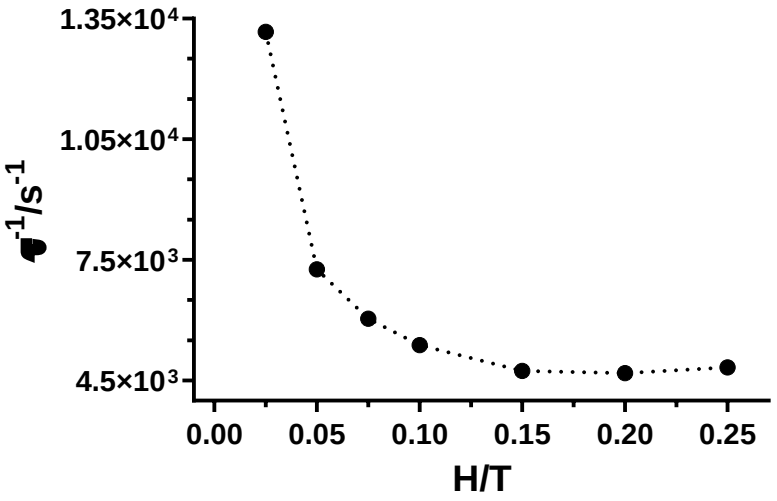

Figure S57.- The inverse of the relaxation times obtained at different magnetic fields at 2.0 K for **3**$_{Y}$.

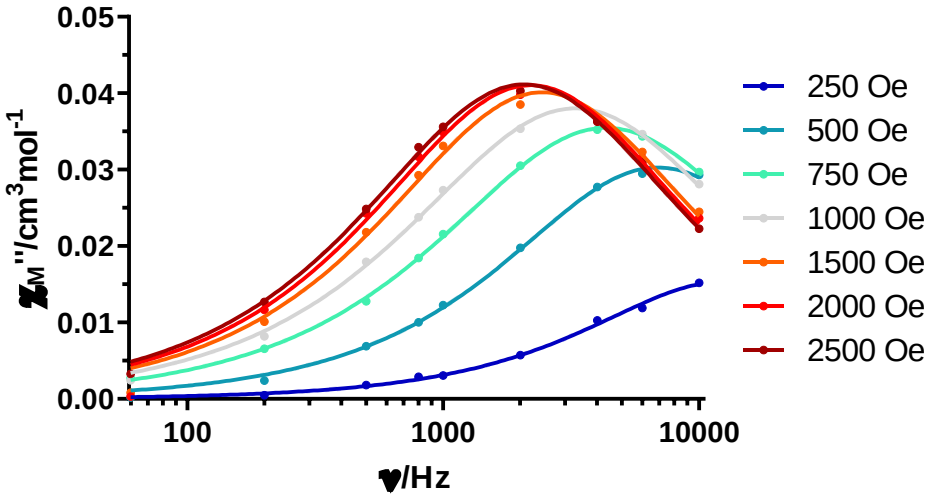

Figure S58.- Field dependence of the out-of-phase signal *vs* frequency at 22.6 K for **3**$_{Y}$.

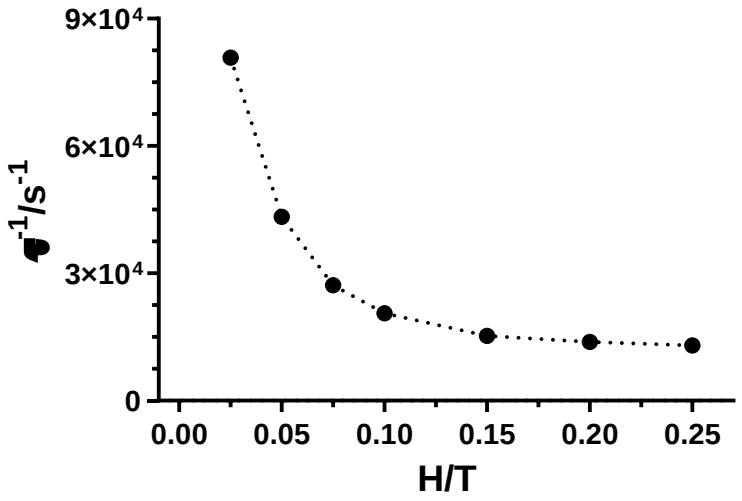

Figure S59.- The inverse of the relaxation times obtained at different magnetic fields at 22.6 K for **3Y**.

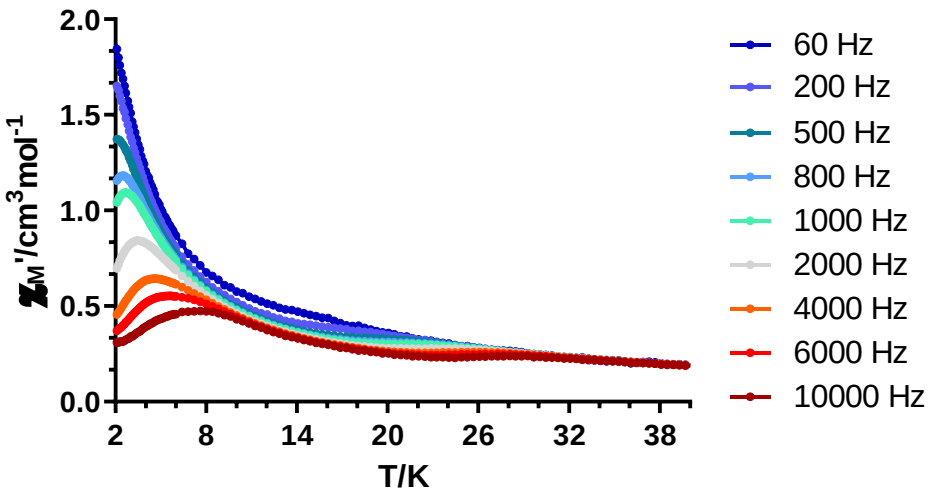

Figure S60.- Temperature dependence of the in phase components of the *ac* susceptibility in a *dc* applied field of 1.5 kOe for **3Y**.

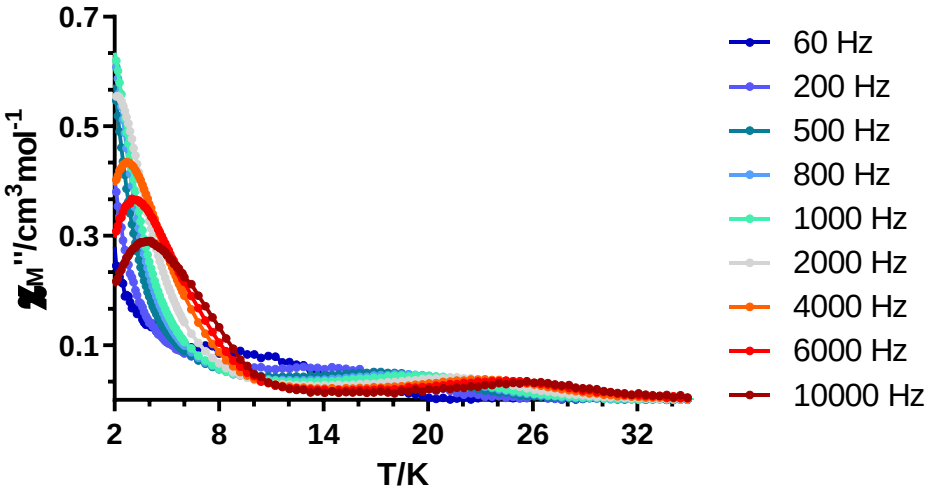

Figure S61.- Temperature dependence of the out-of-phase components of the *ac* susceptibility in a *dc* applied field of 1.5 kOe for **3Y**.

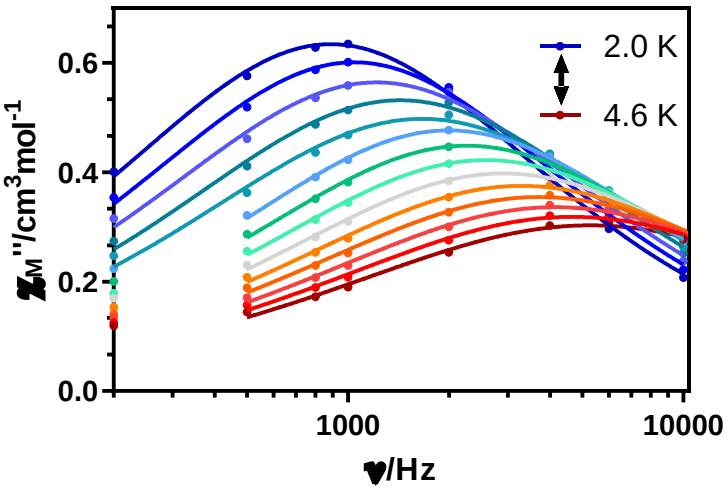

Figure S62.- Variable-temperature frequency dependence of the χ_M'' signal under 1.5 kOe applied field for **3Y**. Solid lines represent the best fitting of the experimental data to the Debye model.

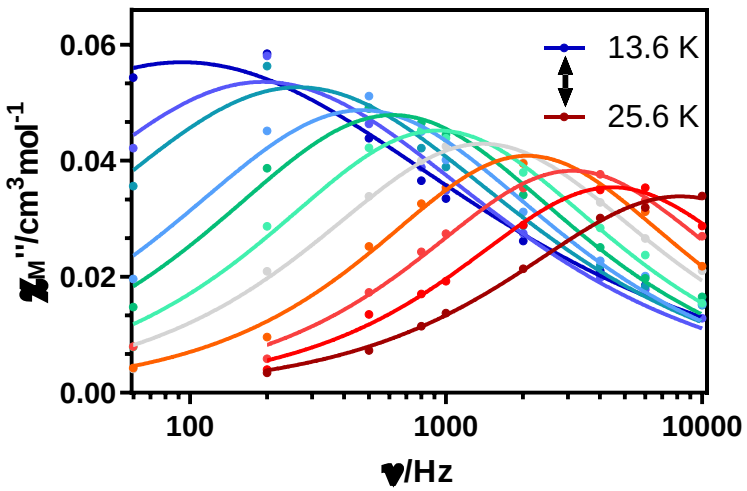

Figure S63.- Variable-temperature frequency dependence of the χ_M'' signal under 1.5 kOe applied field for **3Y**. Solid lines represent the best fitting of the experimental data to the Debye model.

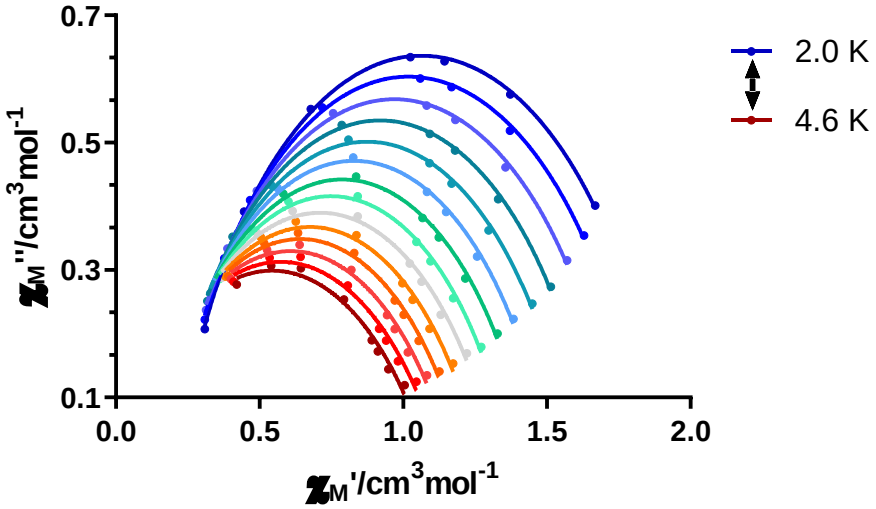

Figure S64.- Cole-Cole plots under 1.5 kOe field for **3Y**. Solid lines represent the best fit to the generalized Debye model.

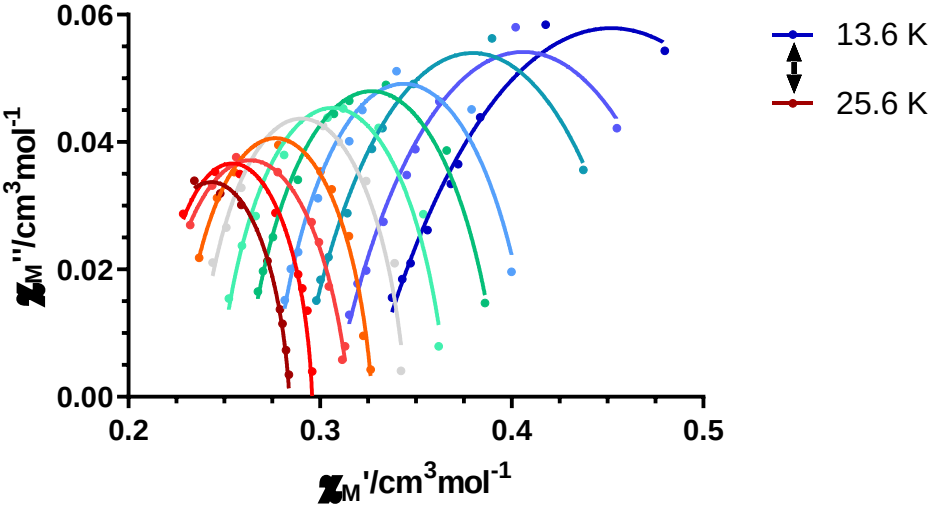

Figure S65.- Cole-Cole plots under 1.5 kOe field for **3Y**. Solid lines represent the best fit to the generalized Debye model.

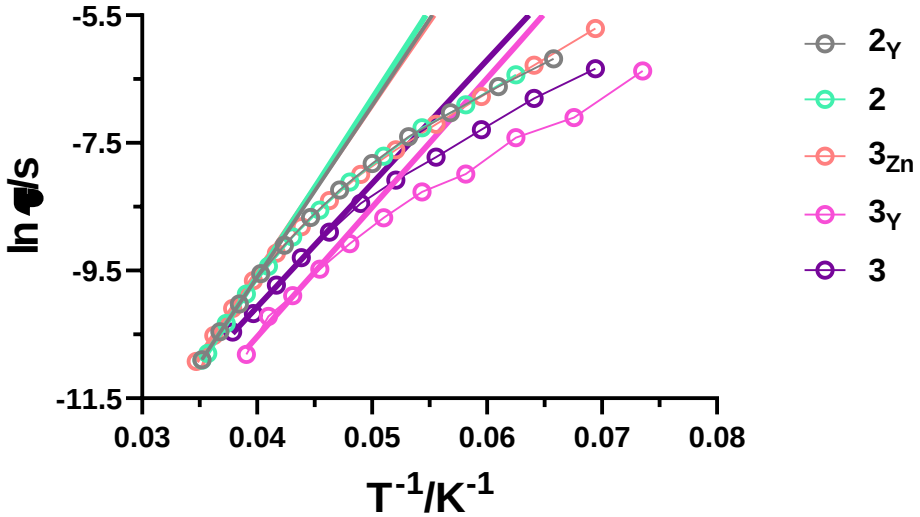

Figure S66.- Arrhenius plots for the relaxation times with Orbach fittings. H_{dc} = 1 kOe for **2** and **2Y**; H_{dc} = 2.5 kOe for **3** and **3Zn**; H_{dc} = 1.5 kOe for **3Y** and.

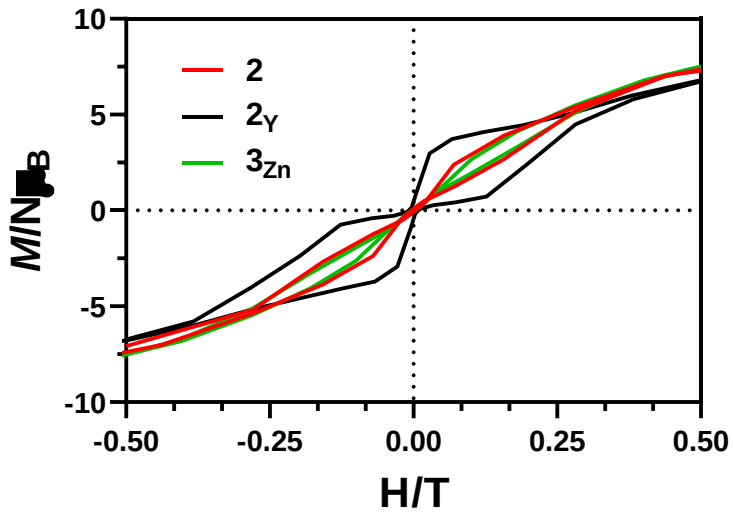

Figure S67.- Magnetic hysteresis loops for **2**, **2Y** and **3Zn** for *H* values between -0.5 T and 0.5 T at 2 K and the sweep rates indicated in the text. Note that the curve for **2Y** has been normalized.

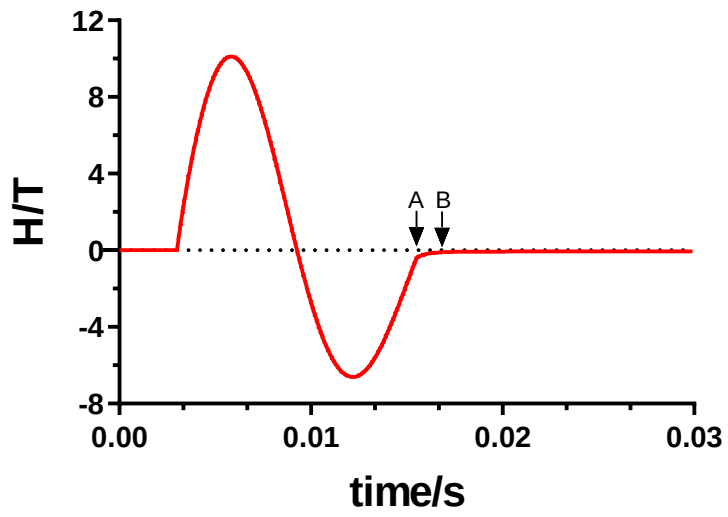

Figure S68.- Field-scan sequence as a function of time for a maximum field of 10.4 T. Note that the pulsed-field magnetization curves in Figure 11 are stopped at B. Thus, the much slower sweep-rates between A and B are responsible of the asymmetric features between the positive and negative parts of the loop.

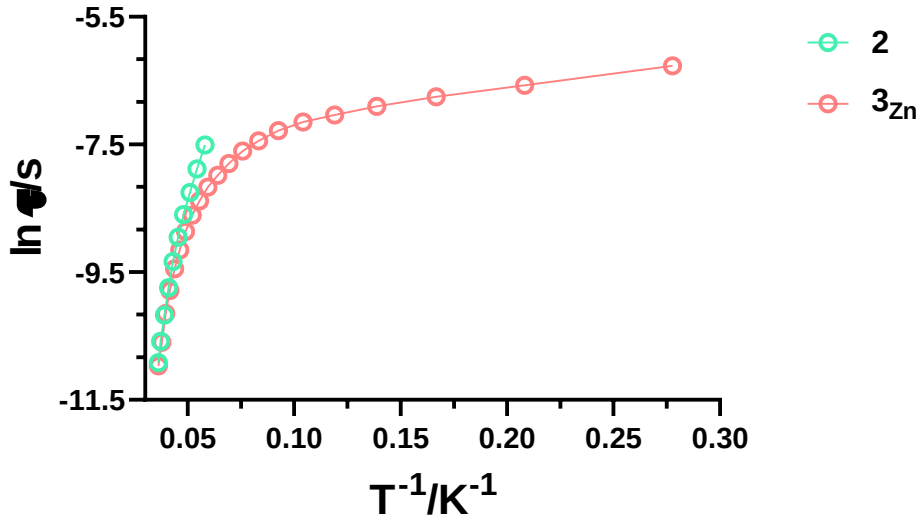

Figure S69.- Arrhenius plots for the relaxation times for **2** and **3$_{Zn}$** under zero applied dc field.

S9.- Theoretical calculations

Table S8.- Decomposition of the wavefunctions of the components of each Kramers' doublet of complex **1'B** into wavefunctions with definite J_z (z is the easy axis for the ground Kramers doublet).

KD	ΔE, cm^{-1} (in K)	$\lvert J_z \rvert$ (contribution in %)
1	0	15/2 (98.6)
2	120 (173)	7/2 (21.8). 5/2 (19.4). 9/2 (17.1). 3/2 (15.6). 1/2 (13.5)
3	198 (285)	13/2 (31.1). 9/2 (20.7). 11/2 (15.4). 7/2 (14)
4	238 (342)	13/2 (50.6). 11/2 (18.1). 7/2 (12.2)
5	294 (423)	11/2 (39.6). 9/2 (21.8). 3/2 (12.3)
6	362 (521)	7/2 (26.3). 9/2 (26.1). 11/2 (17.2). 5/2 (16.1)
7	463 (666)	3/2 (32.8). 5/2 (30.8). 7/2 (17.4). 9/2 (11.7)
8	618 (889)	1/2 (52.9). 3/2 (31.1). 5/2 (11.8)

Table S9.- Decomposition of the wavefunctions of the components of each Kramers' doublet of complex **1'A** into wavefunctions with definite J_z (z is the easy axis for the ground Kramers doublet).

KD	ΔE, cm^{-1} (in K)	$\lvert J_z \rvert$ (contribution in %)
1	0	15/2 (83.8)
2	32 (46)	1/2 (24.4). 3/2 (23.3). 5/2 (16.7). 9/2 (11.6). 7/2 (10.9)
3	133 (191)	13/2 (80.6)
4	221 (318)	11/2 (55.8). 1/2 (9.6)
5	242 (348)	1/2 (22.2). 9/2 (21.5). 11/2 (18.7). 5/2 (18.6)
6	272 (391)	9/2 (26.8). 3/2 (24.9). 7/2 (17.4). 5/2 (17.4)
7	320 (460)	7/2 (33.4). 9/2 (25). 5/2 (20.4)
8	476 (685)	1/2 (32.7). 3/2 (27). 5/2 (19.3). 7/2 (11.7)

Table S10.- The energy splitting of the ground $^6H_{15}$ multiplet and principal values of the g tensors for each Kramers' doublet in **1'B**.

KD	ΔE, cm^{-1}	g_{xx}	g_{yy}	g_{zz}
1	0	0.0074	0.0151	19.7727
2	120	0.2135	0.2467	18.6515
3	198	1.7913	2.3219	13.8311
4	238	2.5216	5.0699	10.1913
5	294	3.5587	3.7956	10.8868
6	362	0.2301	0.5101	15.3401
7	463	0.2470	0.2815	17.2069
8	618	0.0289	0.0650	19.2900

Table S11.- The energy splitting of the ground $^6H_{15}$ multiplet and principal values of the g tensors for each Kramers' doublet in **1'A**.

KD	ΔE, cm^{-1}	g_{xx}	g_{yy}	g_{zz}
1	0	0.2615	1.1106	18.0841
2	32	0.4794	0.6057	17.4440
3	133	0.0448	0.5418	15.8551
4	221	4.5258	5.1975	10.3174
5	242	9.2911	6.0050	0.1615
6	272	1.8452	2.9599	12.5509
7	320	0.6382	1.4935	15.7848
8	476	0.0309	0.0460	19.5742

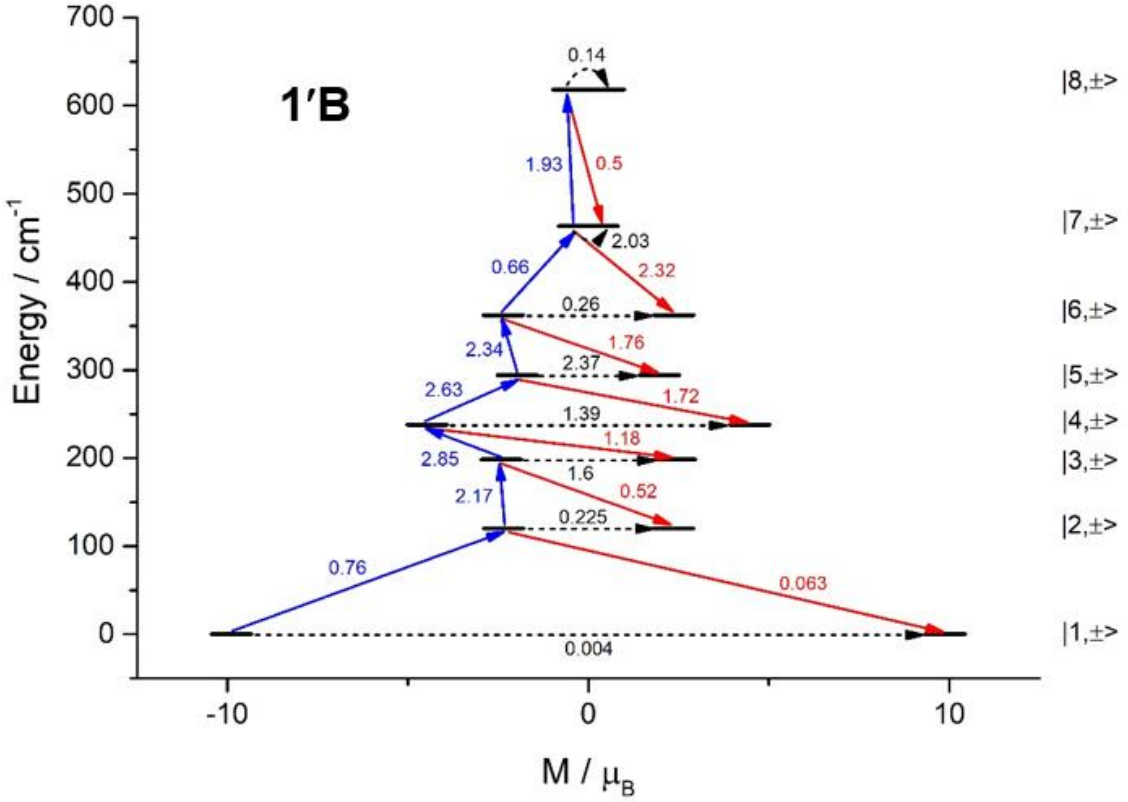

Figure S70.- Magnetization blocking barrier for the complex **1'B**. The exchange states are arranged according to the values of their magnetic moments. The arrows show the connected exchange states, and the numbers at each of them stand for the corresponding matrix element of the transversal magnetic moment.

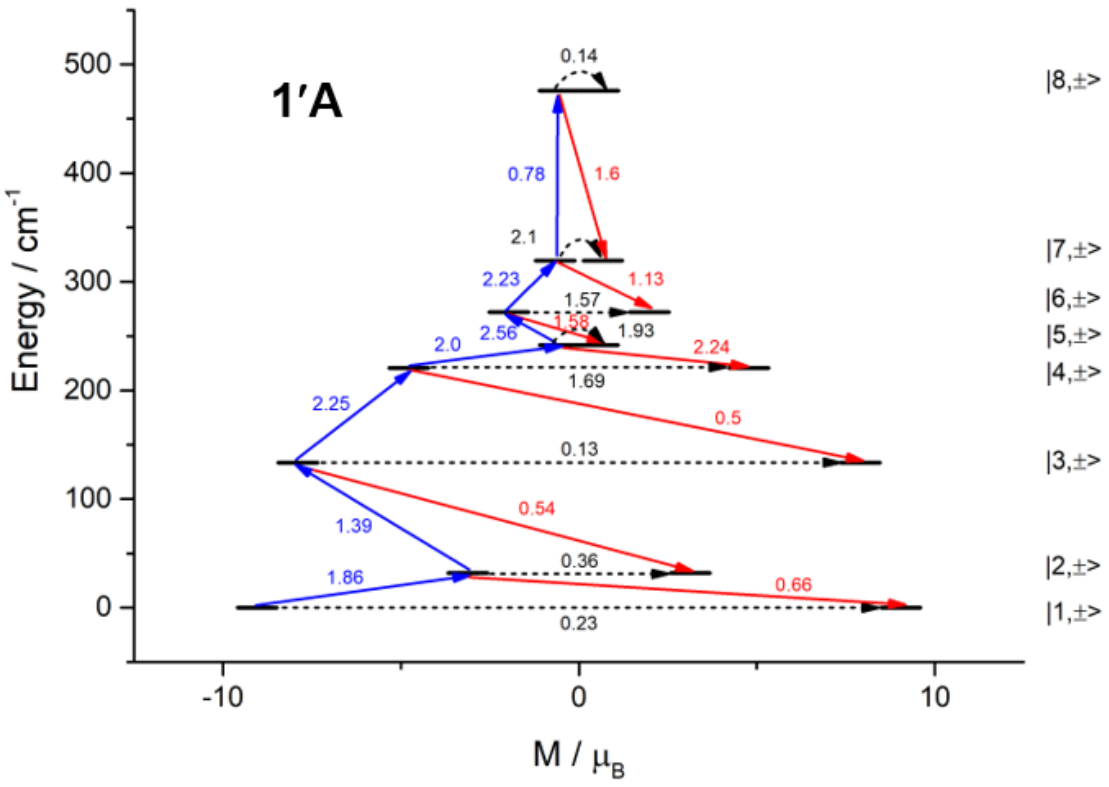

Figure S71.- Magnetization blocking barrier for the complex **1'A**. The exchange states are arranged according to the values of their magnetic moments. The arrows show the connected exchange states, and the numbers at each of them stand for the corresponding matrix element of the transversal magnetic moment.

Table S12.- The Mulliken atomic charges on atoms coordinated to Dy of complex **1'B**. Labels correspond to the ones in the crystal structure. Color code: white = phenoxido; yellow = methoxy; blue = bridging acetate; orange = nitrate; brown = chelating acetate.

Atoms	Mulliken charges
O3B	-1.115
O4B	-0.816
O1B	-1.110
O2B	-0.807
O1D	-0.949
O6B	-0.679
O5B	-0.672
O8B	-1.036
O9B	-0.975

Table S13.- The Mulliken atomic charges on atoms coordinated to Dy of complex **1'A**. Labels correspond to the ones in the crystal structure. Color code: white = phenoxido; yellow = methoxy; blue = bridging acetate; orange = nitrate.

Atoms	Mulliken charges
O1A	-1,1125
O1C	-0,9595
O2A	-0,8125
O3A	-1,1235
O4A	-0,8256
O5A	-0,6709
O6A	-0,6817
O8A	-0,6736
O9A	-0,6538

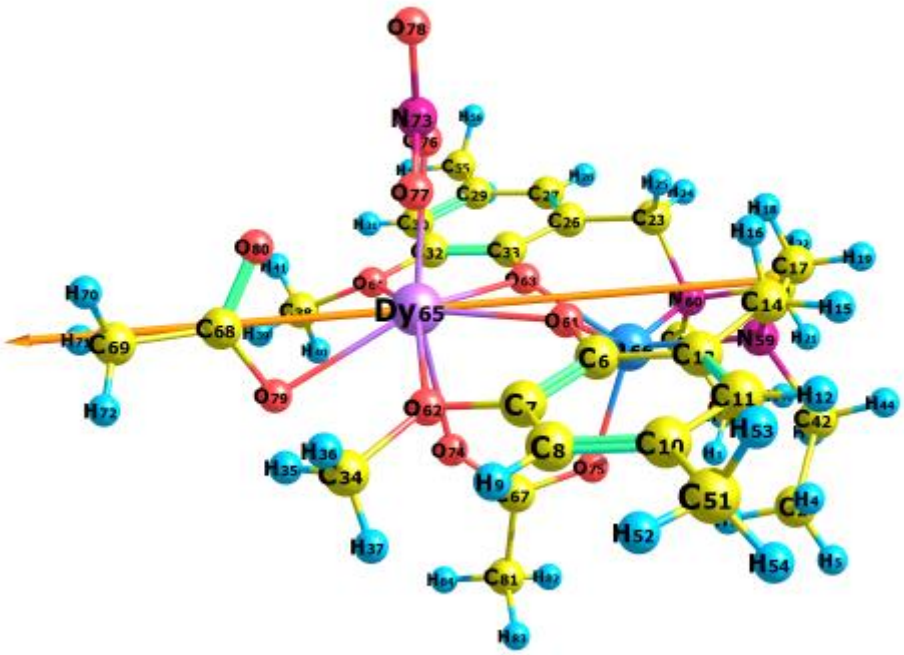

Figure S72.- Direction of the easy axis for **1'B**. Note that the labels do not correspond to the ones in the crystal structure; they were used for computational calculations.

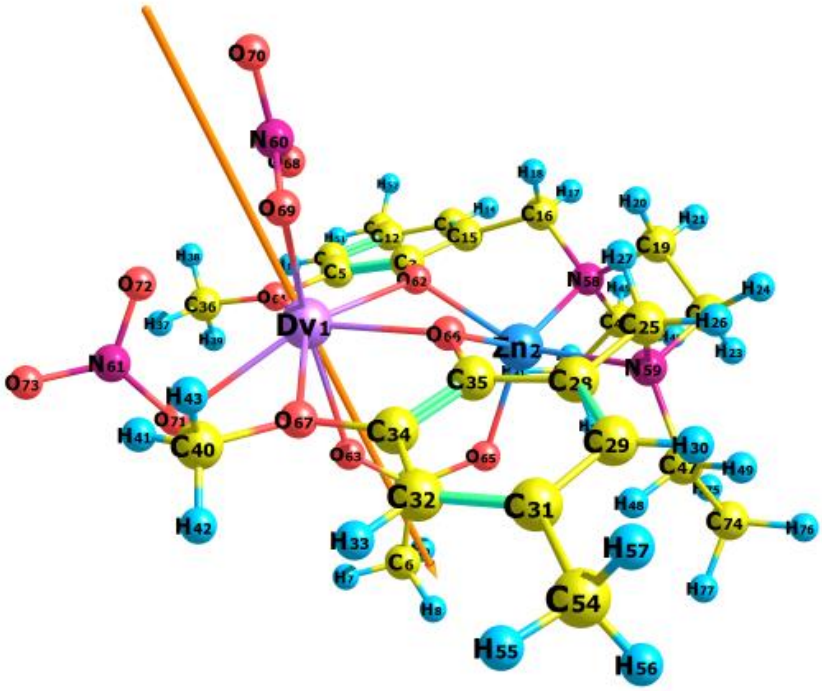

Figure S73.- Direction of the easy axis for **1'A**. Note that the labels do not correspond to the ones in the crystal structure; they were used for computational calculations.

Table S14.- Decomposition of the wavefunctions of the components of each Kramers' doublet of complex **2'** into wavefunctions with definite J_z (z is the easy axis for the ground Kramers doublet).

KD	ΔE, cm^{-1} (in K)	$\|J_z\|$ (contribution in %)
1	0	15/2 (99.6)
2	199 (286)	13/2 (88.3), 11/2 (9.5)
3	326 (469)	11/2 (46.7), 9/2 (23.5)
4	373 (537)	1/2 (26), 11/2 (20.2), 7/2 (18.9), 3/2 (17.6), 5/2 (10.2)
5	453 (652)	9/2 (34.7), 7/2 (20.6), 5/2 (17.1), 11/2 (14.3)
6	542 (780)	7/2 (32.2), 9/2 (31.2), 5/2 (17.6)
7	629 (905)	5/2 (37.7), 3/2 (28.9), 7/2 (23.5)
8	750 (1079)	1/2 (52.1), 3/2 (31.1), 5/2 (11.2)

Table S15.- The energy splitting of the ground $^6H_{15}$ multiplet and principal values of the g tensors for each Kramers' doublet in **2'**.

KD	ΔE, cm^{-1}	g_x	g_y	g_z
1	0	0.0046	0.0054	19.8
2	199	0.081	0.132	17.2
3	326	1.15	2.02	13.2
4	373	0.35	3.5	12.26
5	453	7.19	6.6	5.12
6	542	2.01	2.52	14.35
7	629	0.43	0.72	15.88
8	750	0.07	0.2	18.72

Table S16.- Angles between the main magnetic axes of excited Kramers doublets (KD) and the main magnetic axis of the ground state Kramers doublet for complex **2'**.

KDs	1	2	3	4	5	6	7	8
∠, degrees	0	14.4	32.3	71.2	118.1	113.9	101.1	90.0

Table S17.- The Mulliken atomic charges on atoms coordinated to Dy of complex **2'**. Labels correspond to the ones in the crystal structure. Color code: white = phenoxido; yellow = methoxy; blue = bridging acetate; orange = nitrate.

Atoms	**Mulliken charges**
O7	-1.142
O8	-0.823
O2	-0.809
O2N	-0.690
O4	-0.840
O1S	-1.002
O1	-1.126
O3	-1.129
O1N	-0.686

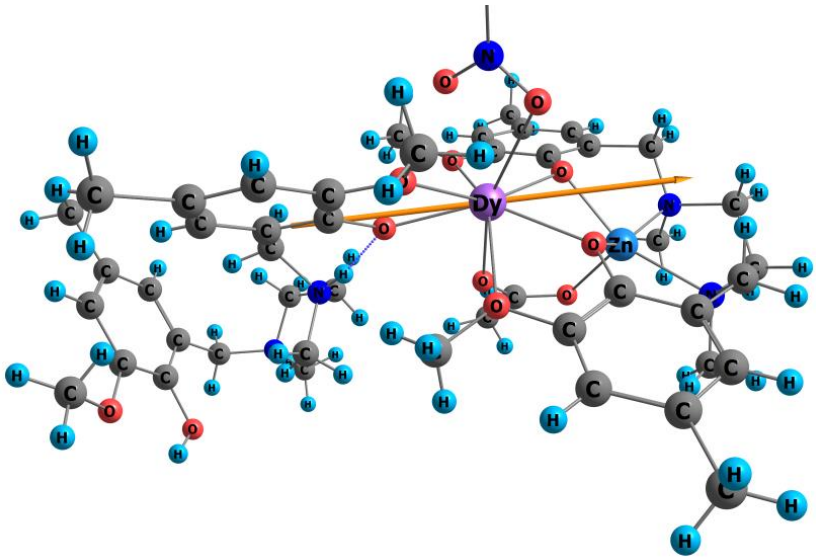

Figure S74.- Direction of the easy axis for **2'**.

Table S18.- Decomposition of the wavefunctions of the components of each Kramers' doublet to the wavefunctions with definite J_z (z is the easy exes for the ground Kramers doublet) for **3'$_{Zn}$**.

KD	ΔE, cm^{-1}	$\lvert J_z \rvert$ (contribution in %)
1	0	**15/2** (99.5)
2	199	**13/2** (89.4), 11/2 (8.3)
3	315	**11/2** (35.5), 9/2 (19.4), 3/2 (14.7), 1/2 (11.2),
4	358	**11/2** (33.9), 1/2 (21), 3/2 (13.6), 7/2 (13.5)
5	443	**9/2 (36.7)**, 7/2 (22.8), 5/2 (14.7), 11/2 (13.6)
6	526	**7/2** (32.4), 9/2 (31.2), 5/2 (18.0)
7	622	**5/2** (37.4), 3/2 (28.6), 7/2 (23.8)
8	754	**1/2** (51.2), 3/2 (31.5), 5/2 (12.0)

Table S19.- Results of calculations at the SA-CASSCF(9,7)/SO-RASSI level using SINGLE ANISO procedure for complex **3'$_{Zn}$**: the energy splitting of the ground $^6H_{15}$ multiplet and principal values of the g-tensor for each Kramers' doublet (KD).

KD	ΔE, cm^{-1}	g_{xx}	g_{yy}	g_{zz}
1	0	0.0047	0.0056	19.7837
2	199	0.1144	0.1886	17.1646
3	315	1.5641	2.7556	13.6952
4	358	0.298	4.3705	10.0866
5	443	7.4605	6.5921	5.1265
6	526	2.0155	2.2854	14.4643
7	622	0.3488	0.5660	16.1748
8	754	0.0624	0.1488	19.0170

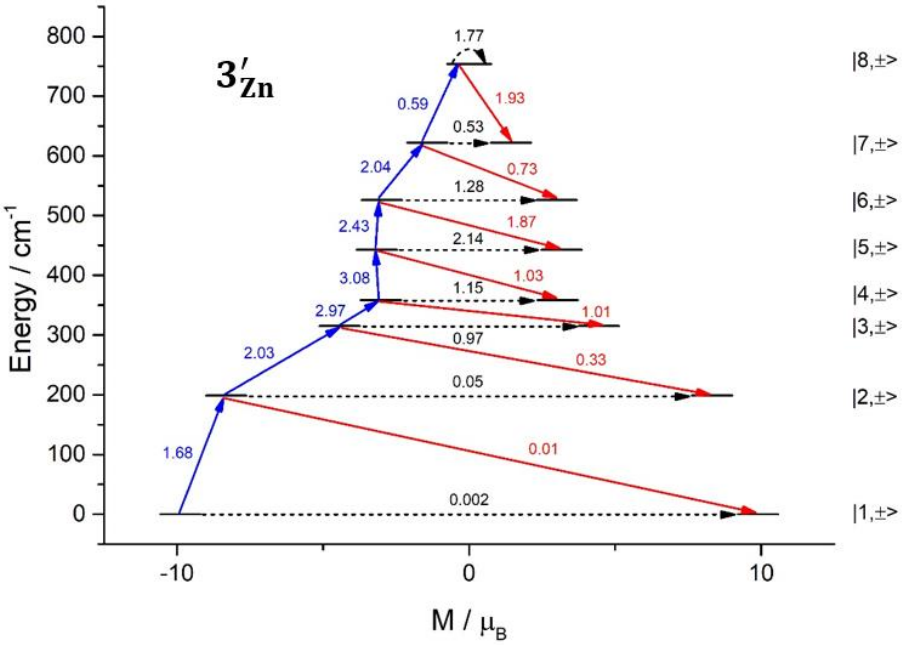

Figure S75.- Magnetization blocking barrier in **3'$_{Zn}$** calculated at the SA-CASSCF(9,7)/SO-RASSI level using the SINGLE-ANISO code. The states are arranged according to the values of their magnetic moments. The arrows show the connected exchange states, and the number at each of them stands for the corresponding matrix element of the transversal magnetic moment.

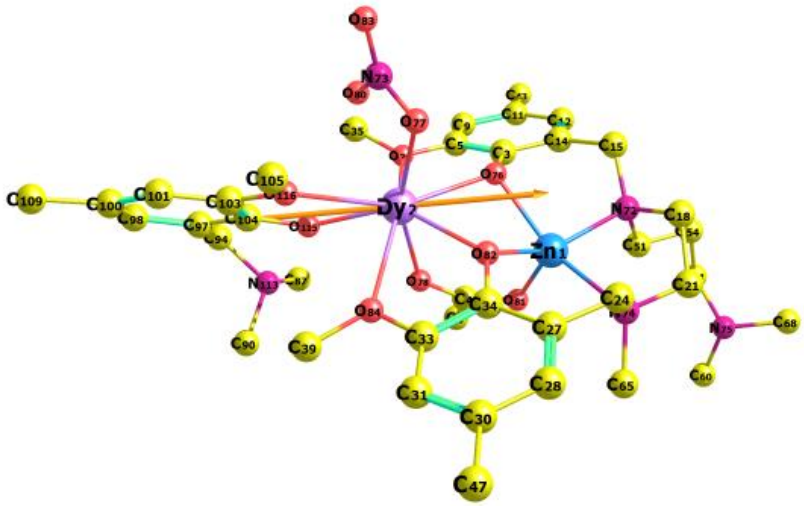

Figure S76.- Direction of the easy axis for **3'$_{Zn}$**.

Table S20.- Compound **3'$_{Y}$** g-tensor of lowest 2 KDs

KD	ΔE. cm^{-1}	g_{xx}	g_{yy}	g_{zz}
1	0	1.5573	2.3567	7.6011
2	134	2.0505	2.4562	5.5668

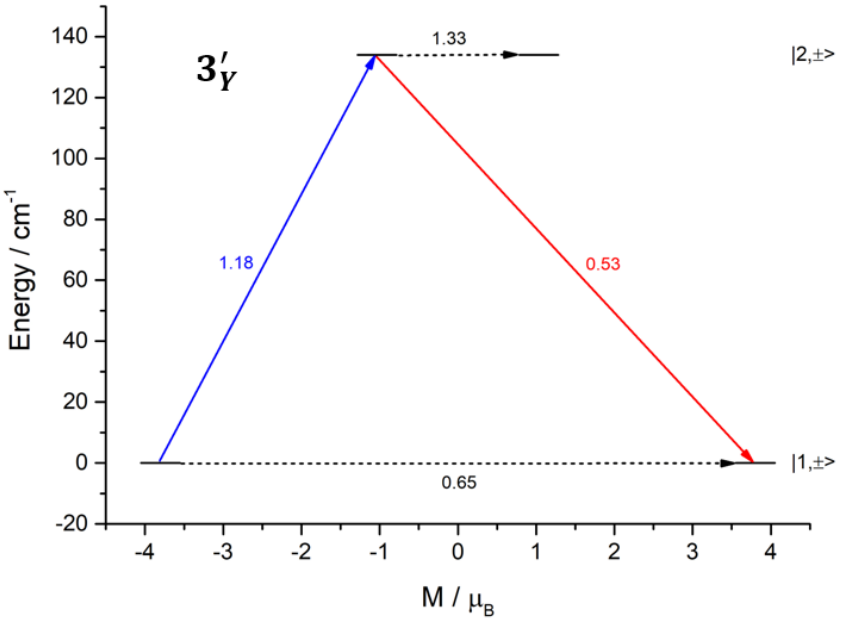

Figure S77.- Magnetization blocking barrier in **3'Y** calculated at the SA-CASSCF(7,5)/SO-RASSI/ANO-RCC-VTZP level using the SINGLE-ANISO code. The states are arranged according to the values of their magnetic moments. The arrows show the connected exchange states, and the number at each of them stands for the corresponding matrix element of the transversal magnetic moment.

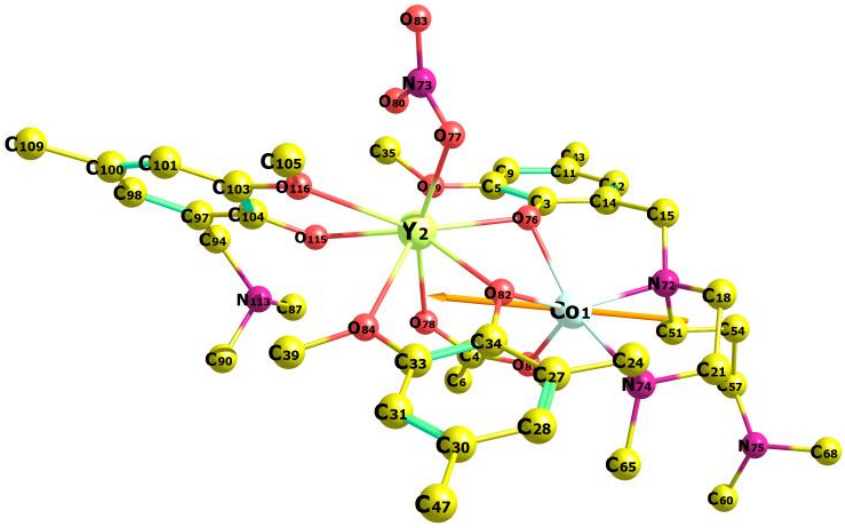

Figure S78.- Direction of the easy axis for **3'Y**.

Table S21.- The energies of the low-lying non-Kramers exchange doublets, their g_{zz} values and tunnelling splitting (ΔE_{tun},) obtained using POLY_ANISO procedure taking into account dipole-dipole and exchange (with J = +0.48 cm^{-1}) interactions leading to the best fit of the temperature dependence of magnetic susceptibility for complex **3'**.

Exchange doublets	< E>, cm^{-1}	ΔE_{tun}, cm^{-1}	g_{zz}	Exchange doublets	< E>, cm^{-1}	ΔE_{tun}, cm^{-1}	g_{zz}
1	0.000	1.33×10^{-4}	24.89	**7**	316.4	0.35	15.23
2	3.023	5.60×10^{-4}	16.46	**8**	317.0	0.51	11.31
3	134.0	2.73×10^{-4}	22.82	**9**	332.9	6.19×10^{-3}	20.34
4	136.1	6.54×10^{-4}	17.41	**10**	334.7	2.12×10^{-2}	14.77
5	199.2	6.51×10^{-3}	21.14	**11**	359.8	0.32	12.78
6	201.3	1.81×10^{-2}	15.48	**12**	360.2	0.24	7.69

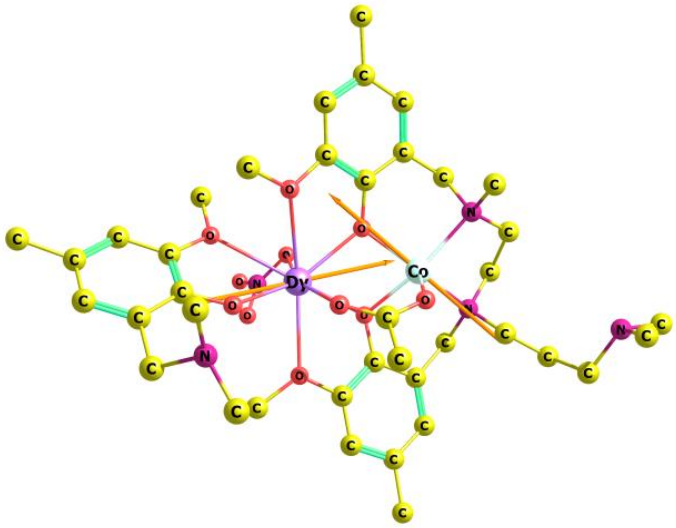

Figure S79.- Direction of the easy axes for **3**, which were calculated separately for **3'$_{Zn}$** and **3'$_{Y}$** units.

S10.- Photoluminescence properties

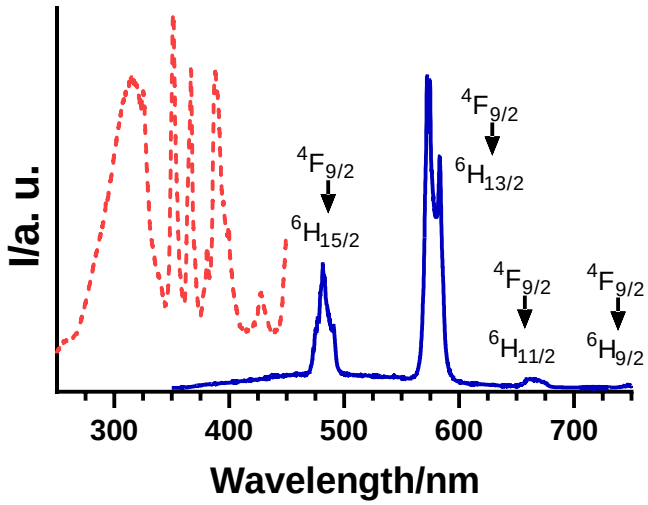

Figure S80.- Solid state photoluminescence excitation (dashed red line) and emission (blue) spectra for powder sample of compound **1**. The excitation spectrum was recorded at room temperature (λ_{em} = 578 nm), whereas the emission spectrum was recorded at 13 K (λ_{ex} = 325 nm).

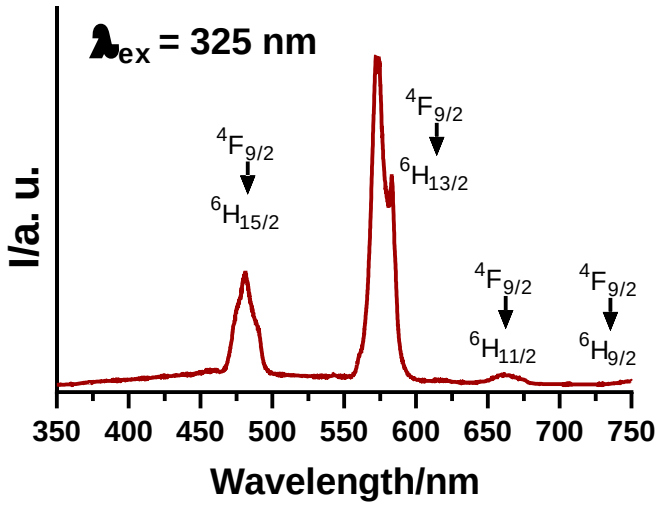

Figure S81.- Solid state photoluminescence emission spectrum for powder sample of compound **1** recorded at room temperature.

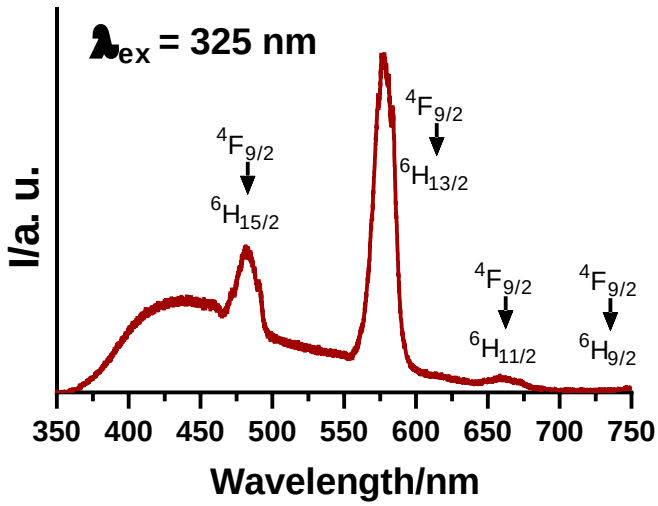

Figure S82.- Solid state photoluminescence emission spectrum for powder sample of compound **2** recorded at room temperature.

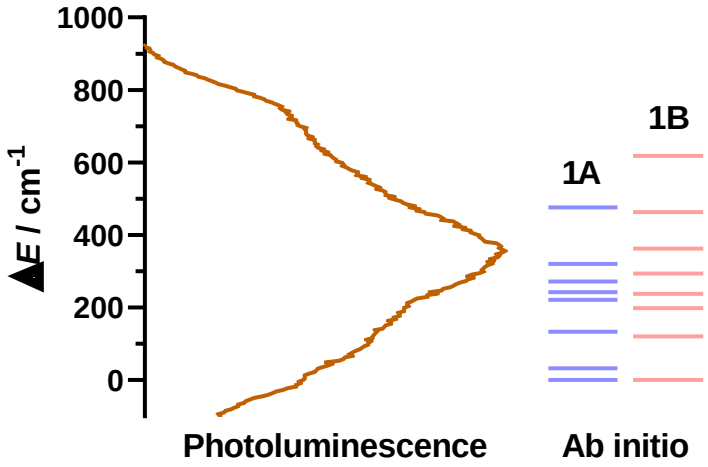

Figure S83.- For compound **1**, room temperature $^4F_{9/2} \rightarrow {}^6H_{15/2}$ emission band in terms of energy (left) and energy values of the Kramers doublets according to ab initio calculations computed for each fragment (right).

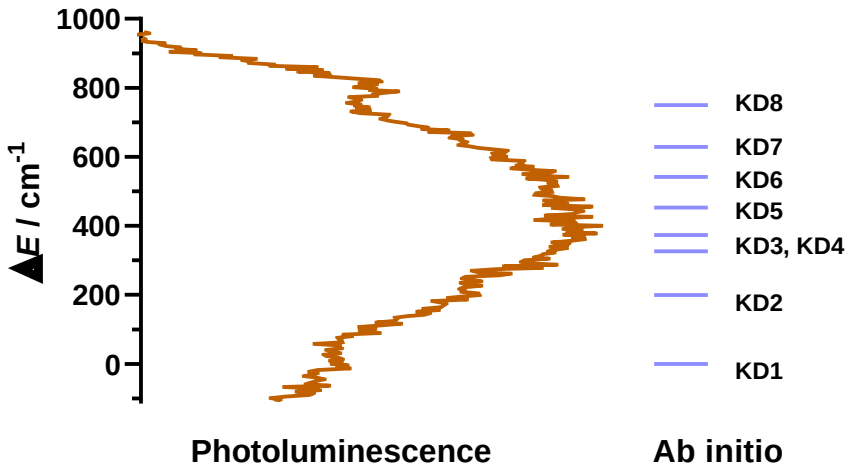

Figure S84.- For compound **2**, room temperature $^4F_{9/2} \rightarrow {}^6H_{15/2}$ emission band in terms of energy (left) and energy values of the Kramers doublets according to ab initio calculations (right).

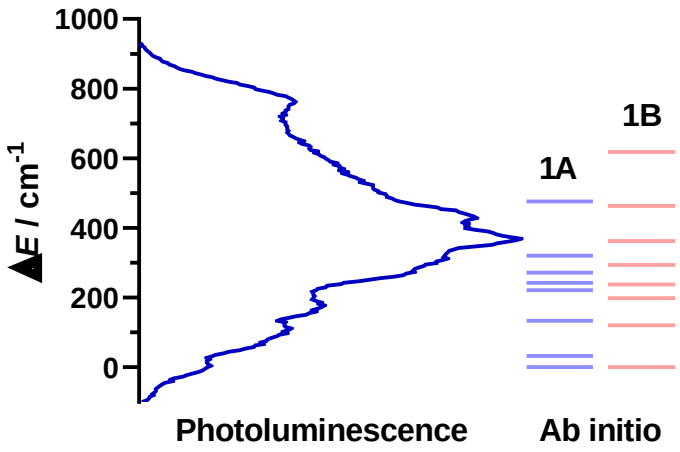

Figure S85.- For compound **1**, 13 K recorded $^4F_{9/2} \rightarrow {}^6H_{15/2}$ emission band in terms of energy (left) and energy values of the Kramers doublets according to ab initio calculations computed for each fragment (right).

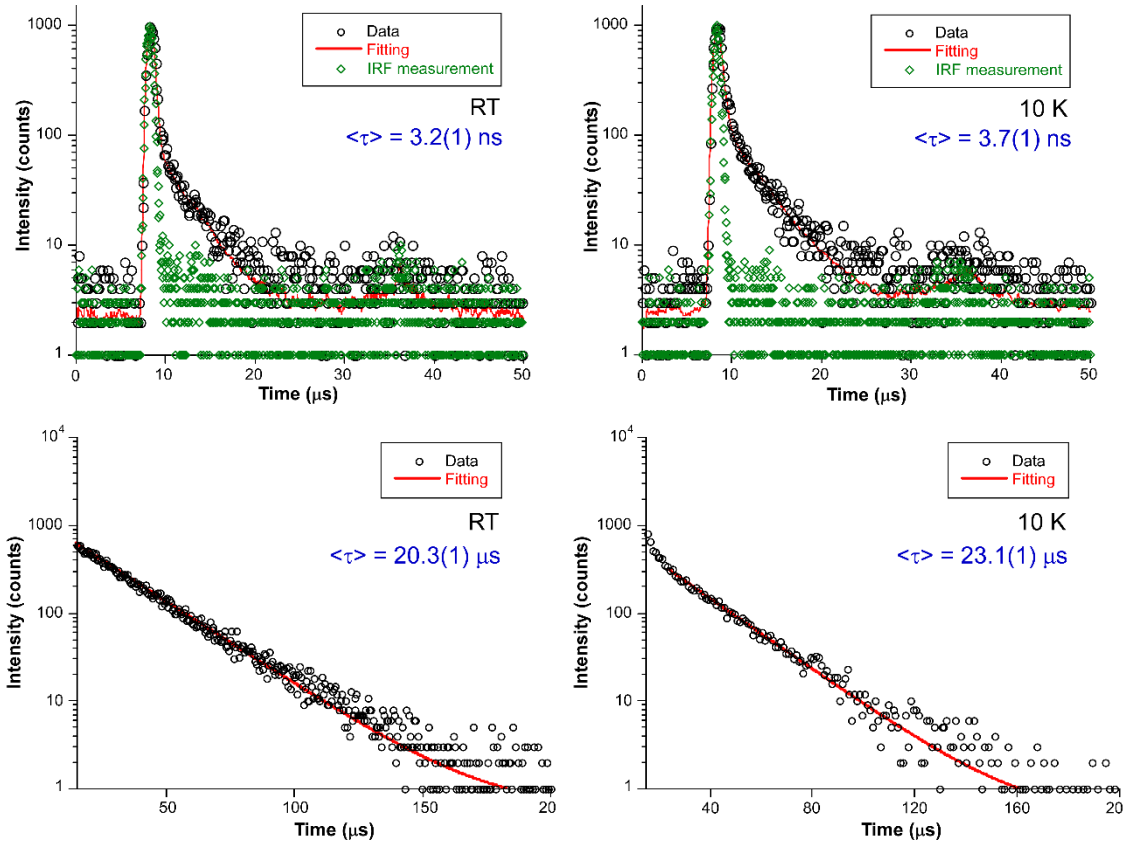

Figure S86.- Emission decay curves fitted for compound **1** at variable temperature.

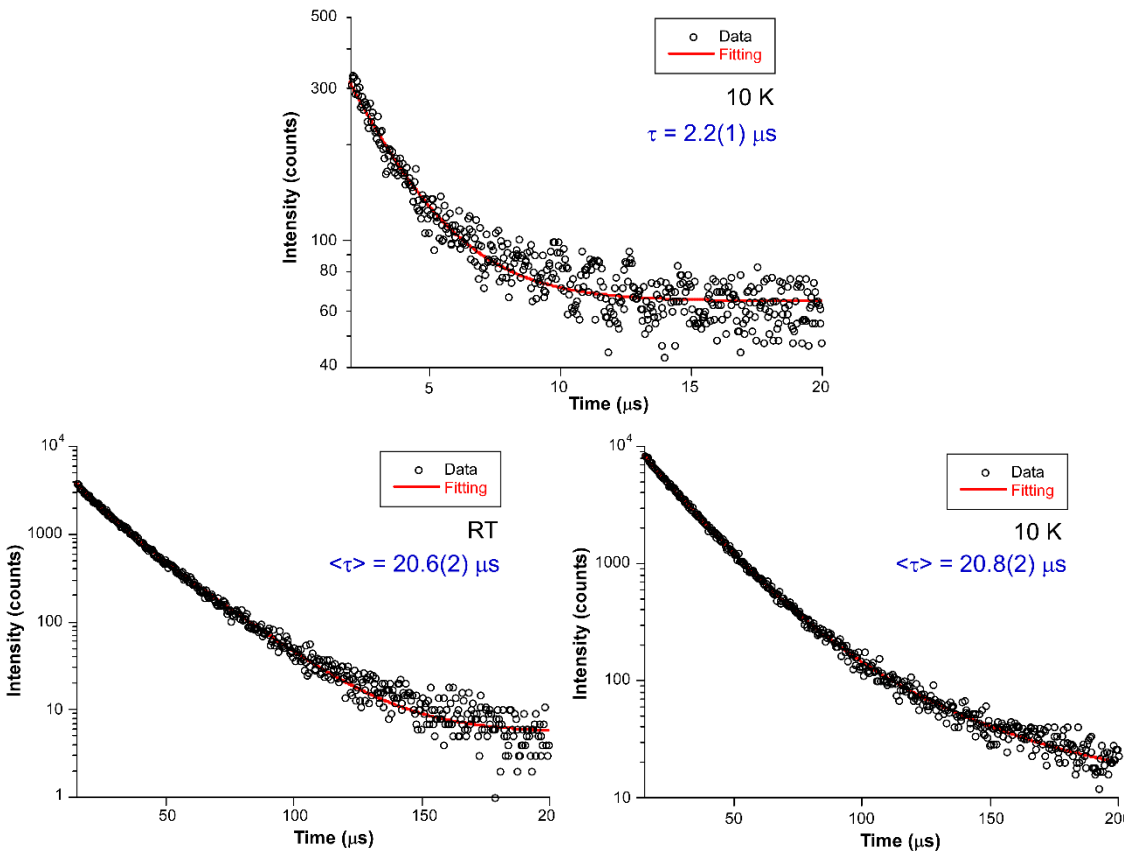

Figure S87.- Emission decay curves fitted for compound **2** at variable temperature.

S11.- Powder X-ray diffraction analysis

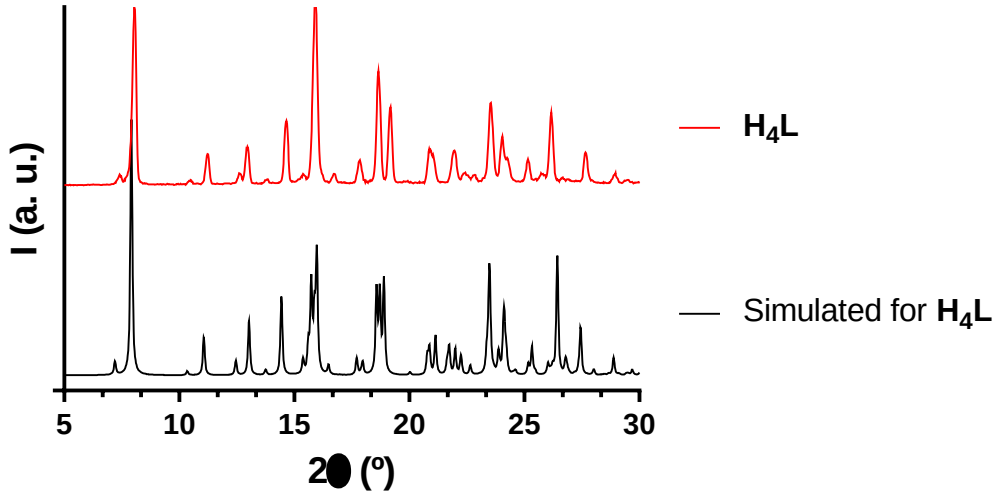

Figure S88.- For H_4L, simulated pattern from single-crystal X-ray diffraction (black line) and experimental XRPD (red).

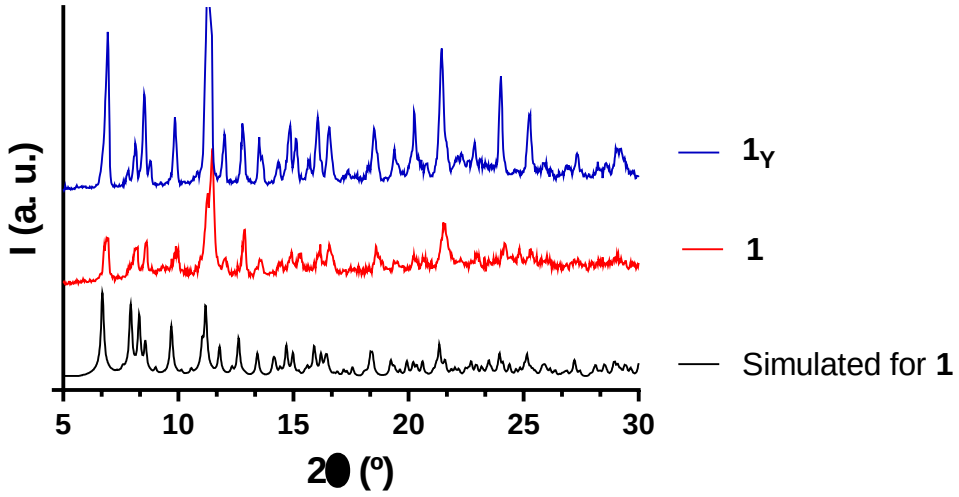

Figure S89.- For **1** and $\mathbf{1_Y}$, simulated pattern from single-crystal X-ray diffraction (black line) and experimental XRPD for **1** (red) and $\mathbf{1_Y}$ (blue).

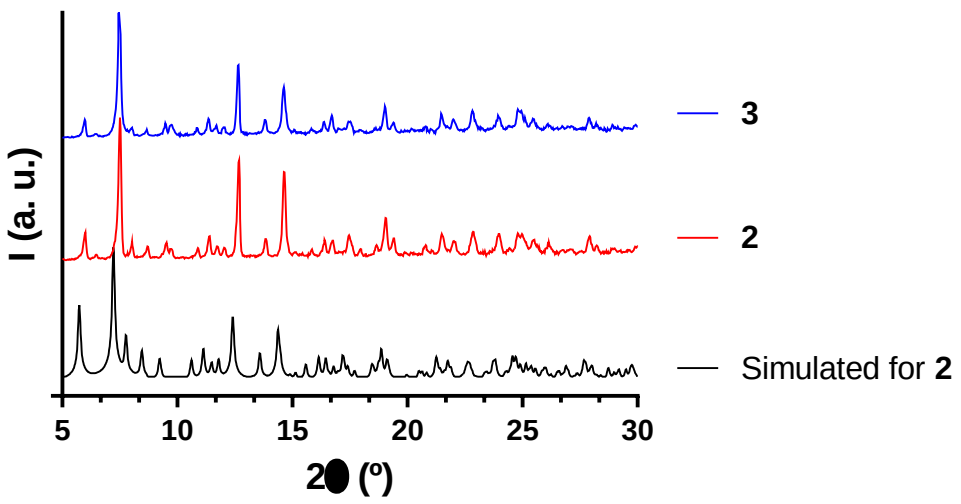

Figure S90.- For **2** and **3**, simulated pattern from single-crystal X-ray diffraction (black line) and experimental XRPD for **2** (red) and **3** (blue).

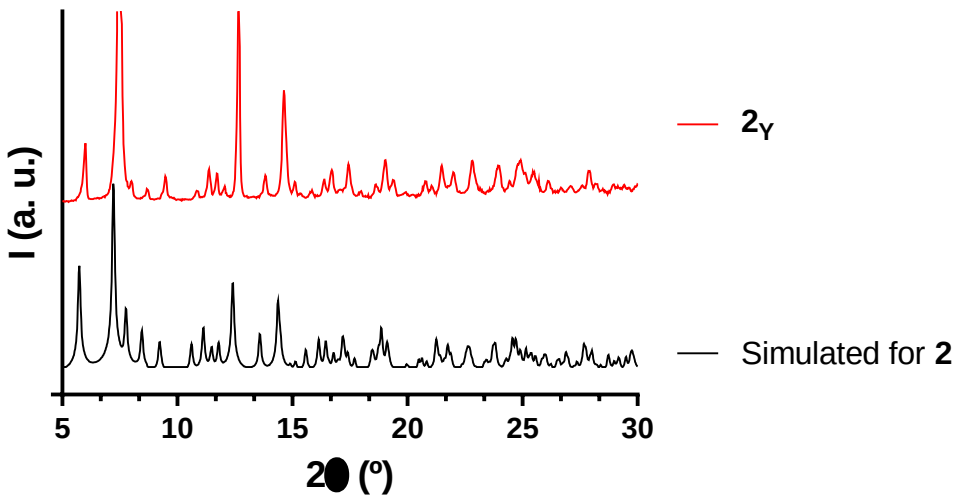

Figure S91.- For **2Y**, simulated pattern from single-crystal X-ray diffraction (black line) and experimental XRPD for **2Y** (red).

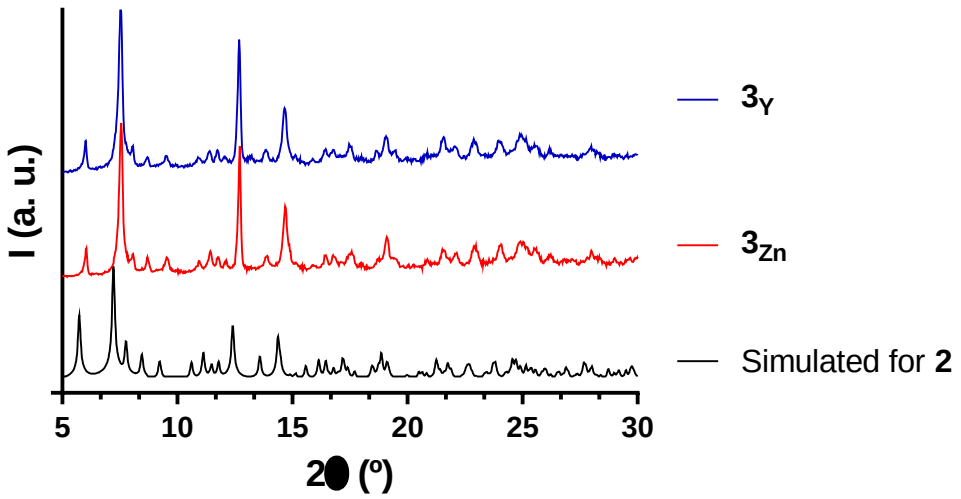

Figure S92.- For **3Zn** and **3Y**, simulated pattern from single-crystal X-ray diffraction (black line) and experimental XRPD for **3Zn** (red) and **3Y** (blue).

S12.- Nuclear Magnetic Resonance

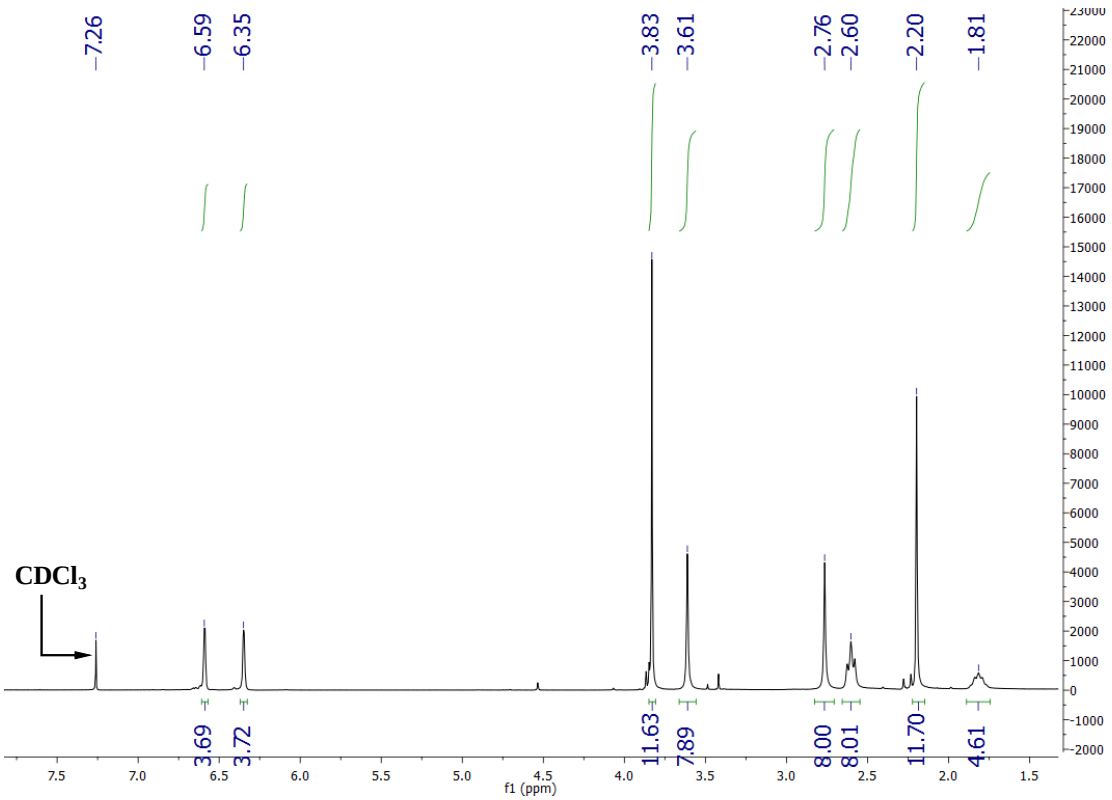

Figure S93.- ^{1}H NMR spectrum for H_4L in $CDCl_3$.

S13.- References

1 A. Earnshaw, *Introduction to Magnetochemistry*, Academic Press, London, 1968.

2 H. Nojiri, K. Y. Choi and N. Kitamura, Manipulation of the quantum tunneling of nanomagnets by using time-dependent high magnetic fields, *J. Magn. Magn. Mater.*, 2007, **310**, 1468–1472.

3 B. A. I. Bruker, *Apex2*, 2004.

4 G. M. Sheldrick, *Program for Empirical Adsorption Correction*, 1996.

5 G. M. Sheldrick, SHELXT – Integrated space-group and crystal-structure determination, *Acta Crystallogr. Sect. A Found. Crystallogr.*, 2015, **71**, 3–8.

6 G. M. Sheldrick, *SHELX-2014, Program for Crystal Structure Refinement*, University of Göttingen: Göttingen (Germany), 2014.

7 L. J. Farrugia, WinGX suite for small-molecule single-crystal crystallography, *J. Appl. Crystallogr*, 1999, **32**, 837–838.

8 F. Aquilante, J. Autschbach, R. K. Carlson, L. F. Chibotaru, M. G. Delcey, L. De Vico, I. Fdez. Galván, N. Ferré, L. M. Frutos, L. Gagliardi, M. Garavelli, A. Giussani, C. E. Hoyer, G. Li Manni, H. Lischka, D. Ma, P. Å. Malmqvist, T. Müller, A. Nenov, M. Olivucci, T. B. Pedersen, D. Peng, F. Plasser, B. Pritchard, M. Reiher, I. Rivalta, I. Schapiro, J. Segarra-Martí, M. Stenrup, D. G. Truhlar, L. Ungur, A. Valentini, S. Vancoillie, V. Veryazov, V. P. Vysotskiy, O. Weingart, F. Zapata and R. Lindh, Molcas 8: New capabilities for multiconfigurational quantum chemical calculations across the periodic table, *J. Comput. Chem.*, 2016, **37**, 506–541.

9 F. Aquilante, J. Autschbach, A. Baiardi, S. Battaglia, V. A. Borin, L. F. Chibotaru, I. Conti, L. De Vico, M. Delcey, I. F. Galván, N. Ferré, L. Freitag, M. Garavelli, X. Gong, S. Knecht, E. D. Larsson, R. Lindh, M. Lundberg, P. Å. Malmqvist, A. Nenov, J. Norell, M. Odelius, M. Olivucci, T. B. Pedersen, L. Pedraza-González, Q. M. Phung, K. Pierloot, M. Reiher, I. Schapiro, J. Segarra-Martí, F. Segatta, L. Seijo, S. Sen, D. C. Sergentu, C. J. Stein, L. Ungur, M. Vacher, A. Valentini and V. Veryazov, Modern quantum chemistry with [Open]Molcas, *J. Chem. Phys.*, 2020, **152**, 214117.

10 P. Å. Malmqvist and B. O. Roos, The CASSCF state interaction method, *Chem. Phys. Lett.*, 1989, **155**, 189–194.

11 P. E. M. Siegbahn, J. Almlöf, A. Heiberg and B. O. Roos, The complete active space SCF(CASSCF) method in a Newton–Raphson formulation with application to the HNO molecule, *J. Chem. Phys.*, 1998, **74**, 2384.

12 F. Aquilante, L. De Vico, N. Ferré, G. Ghigo, P.-å. Malmqvist, P. Neogrády, T. B. Pedersen, M. Pitoňák, M. Reiher, B. O. Roos, L. Serrano-Andrés, M. Urban, V. Veryazov and R. Lindh, MOLCAS 7: The Next Generation, *J. Comput. Chem.*, 2010, **31**, 224–247.

13 B. O. Roos, R. Lindh, K. Malmqvist, V. Veryazov and P.-O. Widmark, Main Group Atoms and Dimers Studied with a New Relativistic ANO Basis Set, *J. Phys. Chem. A*, 2004, **108**, 2851–2858.

14 M. Douglas and N. M. Kroll, Quantum electrodynamical corrections to the fine structure of helium, *Ann. Phys.*, 1974, **82**, 89–155.

15 B. A. Hess, Relativistic electronic-structure calculations employing a two-component no-pair formalism with external-field projection operators, *Phys. Rev. A*, 1986, **33**, 3742.

16 P. Å. Malmqvist, B. O. Roos and B. Schimmelpfennig, The restricted active space (RAS) state interaction approach with spin–orbit coupling, *Chem. Phys. Lett.*, 2002, **357**, 230–240.

17 B. O. Roos and P. Å. Malmqvist, Relativistic quantum chemistry: the multiconfigurational approach, *Phys. Chem. Chem. Phys.*, 2004, **6**, 2919–2927.

18 L. F. Chibotaru and L. Ungur, Ab initio calculation of anisotropic magnetic properties of complexes. I. Unique definition of pseudospin Hamiltonians and their derivation, *J. Chem. Phys.*, 2012, **137**, 064112.

19 L. Ungur and L. F. Chibotaru, *Computational Modelling of the Magnetic Properties of Lanthanide Compounds*, John Wiley & Sons, Ltd, 2015.

20 L. Ungur and L. F. Chibotaru, *POLY_ANISO program*, KU Leuven: Leuven, Belgium, 2007.

21 M. E. Lines, Orbital Angular Momentum in the Theory of Paramagnetic Clusters, *J. Chem. Phys.*, 2003, **55**, 2977.